Deep Iterative Convergence of RANS methods for High-Lift aircraft geometries

Baptiste Arnould * and Éric Laurendeau†
Polytechnique Montréal, Montréal, Canada, H3T IJ4

The fifth edition of the High-Lift Prediction Workshop (HLPW5) was organized to evaluate the CFD community's capability to accurately predict flows and aerodynamic loads in complex high-lift configurations. While the workshop led to significant progress, several questions remained unanswered, and recurring challenges persisted across multiple editions. The complex geometries introduced by high-lift devices, such as slats, flaps, and their associated brackets, lead to the formation of large separation regions in Reynolds-Averaged Navier-Stokes (RANS) solutions that are not observed in experimental oil-flow visualizations. Furthermore, the emergence of these large separation areas compromises the ability of RANS solvers to achieve deep iterative convergence. Addressing and overcoming these challenges is a critical step toward ensuring consistency and alignment across different CFD RANS solvers. To tackle this issue, the present work focuses on one of the challenges raised by the HLPW5 RANS Technology Focus Group: achieving iteratively converged solutions for complex high-lift configurations. This is accomplished through the successful application of the Selective Frequency Damping Method, which enables RANS solvers to converge toward unstable equilibrium solutions. Additionally, this study presents observations regarding the pseudo-unsteady nature of the large separation regions identified in the RANS solutions.

Nomenclature

C_L = lift coefficient

C_D = drag coefficient

C_{My} = pitching moment coefficient

q = flow state

$\overline{q}$ = low-pass time-filtered flow state

r = number of iterations between every reset of the filtered flow

*PhD Student, Department of Mechanical Engineering, Polytechnique Montréal, baptiste.arnould@polymtl.ca, AIAA Student Member
†Professor, Department of Mechanical Engineering, Polytechnique Montréal, eric.laurendeau@polymtl.ca, AIAA Senior Member
This paper includes content that was previously presented at the AIAA SciTech Forum, January 6–10, 2025, in Orlando, Florida (AIAA Paper No. 2025-0279).

α = angle of attack

Δ = filter width of the Selective Frequency Damping Method

χ = control coefficient of the Selective Frequency Damping Method

I. Introduction

Predicting the maximum lift coefficient of an aircraft remains a significant challenge in the aerospace industry, primarily due to the complex physics involved, such as early boundary layer separation, extensive regions of separated flow, and the intricate geometries of high-lift devices. To address these challenges and evaluate the predictive capabilities within the Computational Fluid Dynamics (CFD) community, the AIAA CFD High-Lift Prediction Workshop (HLPW) series was established to guide advancements in CFD methodologies. The most recent edition of this workshop, the fifth in the series, brought together researchers for a year and a half to focus on three main test cases. Test Case 1, a verification study, considered a simple wing-body configuration and focused on grid convergence for lift, drag, and pitching-moment coefficients. Test Case 2 was a configuration buildup study that examined the effects of increasing geometric complexity, including configurations with slats, flaps, and a nacelle/pylon (Configurations 2.2, 2.3, and 2.4). Finally, Test Case 3 investigated the reference landing configuration under four Reynolds number conditions: 1.05 million, 5.49 million, 16 million, and 30 million. This fifth edition of the workshop led to significant advancements in the understanding of high-lift configuration flows. However, several questions remained unresolved. The summary published by the Reynolds-Averaged Navier–Stokes (RANS) Technology Focus Group (TFG) at the conclusion of the event effectively highlights various open topics that require further investigation by the community [1], including: i) isolating bracket-geometry issues from the ability to predict separated flows, and ii) modifying RANS models, grids, and solvers to demonstrate iterative convergence or developing solver technologies capable of achieving iterative convergence for complex flows.

These points highlight a perplexing observation: when high-lift devices are deployed alongside their respective brackets, large separation regions, commonly referred to as "pizza slices," are predicted by RANS solvers [2]. However, these regions are either absent or significantly smaller in oil-flow images from experimental campaigns [3]. Moreover, the emergence of these large separation regions is closely linked with the inability of RANS solvers to converge to steady-state solutions with machine-level accuracy. Indeed, the workshop summary of the RANS TFG [1] reports that while good iterative convergence was achieved for Test Cases 1 and 2.1, Test Case 2.2 presented greater challenges due to the introduction of slats and their brackets. As the geometric complexity increased, iterative convergence for Test Cases 2.3 and 2.4 was reported to be even more difficult or even impossible, due to the emergence of "pizza-slice" disturbances identified as the primary barrier to convergence. For Test Cases 3.1, 3.2, 3.3, and 3.4, no iterative convergence was achieved at all, with such convergence proving elusive for these complex configurations. This widespread struggle

among RANS solvers to reach deep iterative convergence highlights a critical avenue for future research: improving solver methodologies and developing advanced technologies to enable and demonstrate robust iterative convergence for complex flows and geometries representative of high-lift cases. Addressing and overcoming this challenge represents a critical step toward achieving consistency and alignment across different CFD RANS solvers.

Moreover, beyond facilitating code-to-code verification—by reducing and isolating errors related to iterative convergence from griding errors, discretizations errors, or turbulence modeling errors—converged steady-state solutions also grant access to unstable equilibrium states. Another motivation for computing such solutions lies in their central role in Global Stability Analysis (GSA), a framework specifically designed to investigate the dynamics of unstable flows. GSA offers a robust alternative to unsteady RANS (URANS)-based approaches for predicting both the onset and the characteristics of large-scale flow unsteadiness [4–6]. In this context, the steady solution—commonly referred to as the base flow—serves as the reference state around which small perturbations are introduced and analyzed. However, obtaining such base flows is often challenging, as conventional steady-state solvers tend to diverge from these unstable solutions and instead enter unsteady regimes. To overcome this limitation, it is relevant to seek for methods helping to achieve machine-zero residual convergence solutions.

To that end, this work builds on previous results obtained during High-Lift Prediction Workshop 5 (HLPW5) [2], aiming to expand upon the observations made during that event. Specifically, it seeks to address the iterative convergence issues that were commonly observed and reported by the majority of workshop participants. First, results from Test Case 2 and Test Case 3 of the HLPW5 are presented as a foundation for the analysis and developments discussed in this paper. Second, the Selective Frequency Damping (SFD) method is introduced as a relevant and effective approach in light of the observations made in Sec. III. Finally, an analysis of the results obtained using the SFD method is provided. These results aim to advance the capabilities and understanding of the community regarding the complex flows characteristic of high-lift configurations. While this work brings a new perspective on the nature and mechanisms hidden behind the expression "pizza slices," it does not claim to resolve all the questions surrounding these large separation regions, especially the reasons for their formation. Nonetheless, this contribution sheds light and provides means to answer several questions raised by the HLPW5 committee.

II. Numerical methods

All the simulations in this work were performed using the CHAMPS solver. CHAMPS (CHApel Multi-Physics Simulation) is a software developed at Polytechnique Montréal for aerodynamic [7], aero-elastic, and aero-icing simulations. It features classic compressible RANS-based algorithms but is implemented in the new programming language Chapel [8], which provides an alternative to the classic OpenMP and MPI parallelization paradigms for parallel computing. To the authors' knowledge, CHAMPS is the first CFD solver written using the Chapel language and stands as the largest software developed using this programming language ($\approx 150,000$ lines of code).

Aerodynamic simulations are carried out using a cell-centered finite volume method. For this study, a second-order Roe scheme is used to discretize the convective fluxes of the RANS equations. The second-order scheme uses the piecewise linear reconstruction strategy. The gradients are computed using the Green-Gauss method, with a Venkatakrishnan limiter [9] applied to enhance stability during the initial stages of the simulation. To mitigate its dissipative effects, the limiter is gradually relaxed as the solution converges. This transition explains the presence of residual spikes observed in the iterative convergence of the results presented in this study. The standard Spalart-Allmaras (SA) [10] model is used for all cases, and the convective fluxes of the turbulence model are discretized using a first-order upwind scheme. The RANS equations and turbulence model are solved in a segregated approach and are both iterated using local time-stepping (LTS), through an implicit Euler scheme. The local-time step used in this work is computed using the formulation derived by Mavriplis and Jameson [11] for Navier-Stokes equations on unstructured grids, based on a sum of the convective and viscous spectral radii over all faces of the control volume. The resulting linear systems of equations are solved using a Block Symmetric Gauss-Seidel (BSGS) method. When a full sweep of the angle of attack is considered, a classic warm start from the solutions at a previous angle of attack on the polar is used. Otherwise, for single angle-of-attack runs, a cold start strategy is used (i.e., initializing from freestream conditions).

The whole set of simulations is performed using the committee-supplied grids from Pointwise. For Test Case 2, the mixed-element unstructured-grid family 2.R.03 is used, but due to the limited amount of computational resources, only mesh B of this grid family was used (118 and 148 million cells, respectively, for configurations 2.2 and 2.3). For the same reasons, simulations for Test Case 3 were performed using mesh A from the mixed-element unstructured-grid family 3.R.01 (58, 62, and 64 million cells, respectively, for the Reynolds-number flow conditions 3.2, 3.3 and 3.4).

III. Results and Observations from the High-Lift Prediction Workshop 5

Results obtained during the 5th High Lift Prediction Workshop [2] are presented in this section to introduce the problem and discuss preliminary observations. Here, only Test Cases 2.2 and 2.3, and the entire Test Case 3, will be covered, as these are the most relevant to this work. As a reminder, Test Case 2 is a configuration buildup case, studying the wing-body-slat configuration with horizontal and vertical (HV) stabilizers (Test Case 2.2), and the wing-body-slat-flaps configuration with HV stabilizers (Test Case 2.3) on a polar sweep ranging from 6° to 23.8°. On the other hand, Test Case 3 aims to identify the impact of increased Reynolds number on the aerodynamic loads of a Wing-Body-Slat-Flaps-Nacelle configuration on a polar sweep ranging from 6° to 22°. For these cases, emphasis is placed on the iterative convergence of the residuals and aerodynamic coefficients; therefore, no qualitative discussion on the aerodynamic coefficients' values will be provided. Such analysis is presented in [2].

A. Test Case 2 results

As detailed in the workshop summary, Test Case 2.2 results (see Fig. 1a and Fig. 2) show that achieving iterative convergence is challenging, which is associated with the introduction of slats and slat brackets. At 10° and 12° angle of attack, the iterative convergence plots suggest that with additional iterations, the residual values could have reached lower values. Otherwise, CHAMPS quickly enters into limit cycles.

For Test Case 2.3, similar trends to those observed in Test Case 2.2 emerge (see Fig. 1b and Fig. 3). At higher angles of attack, intriguing observations arise (see Fig. 4). Starting around 14°, "pizza slices" emerge from the outboard slat brackets. These formations, corresponding to large regions of separation, were reported by most of the participants. Initial discussions among the participants suggest that these may be linked to under-resolved mesh on the slat brackets; however, conclusions about the cause of these extensive separation regions remain to be made. These large separation regions also appear in the experimental oil flow visualizations from ONERA [3], though they develop at higher angles of attack and on a smaller scale. Figure 4 shows the surface friction coefficient at various angles of attack for Test Case 2.3 alongside the oil flow visualization from ONERA, illustrating the development of the "pizza slice" as the angle of attack increases. Simulation results show that, with higher angles of attack, these regions expand and increase in number, with additional inboard pizza slices appearing. These observations are not supported by the oil flow visualizations. Moreover, Fig. 4 displays the development of a large inboard separation zone at the root of the wing at $\alpha = 23.5°$, larger than the one observed in the oil flow visualizations.

The results from Test Cases 2.2 and 2.3 underscore the significant challenges faced not only by CHAMPS but also by other participants [1] in accurately matching wind tunnel experimental data for high-lift configurations and flows. These discrepancies may be multifactorial, arising from issues such as mesh quality, lack of mesh refinement, and the limitations of RANS turbulence models, which are known to perform inadequately in cases involving large separated flow regions.

B. Test case 3 results

Concerning Test Case 3, since this test case uses nearly the same geometry as configuration 2.4, with the empennage excluded, similar convergence challenges to those encountered in the previous test case were expected—and indeed encountered. As shown in Fig. 5, the solver quickly enters limit cycles in its residual convergence, a pattern also evident in the iterative convergence of the aerodynamic coefficients (see Fig. 6, Fig. 7, and Fig. 8). While the solver did not converge to low residuals, the aerodynamic coefficients still managed to reach limit cycles that oscillate consistently around a mean value. As observed in Test Case 2.3, this test case also features "pizza slice" structures originating from the slat brackets. Figure A1 in Appendix illustrates how these structures evolve with increasing Reynolds numbers. Notably, as the Reynolds number increases, the size of the pizza slices decreases. This effect is particularly evident at $\alpha = 20°$, where the outermost pizza slices become thinner. Furthermore, some pizza slices observed at a Reynolds

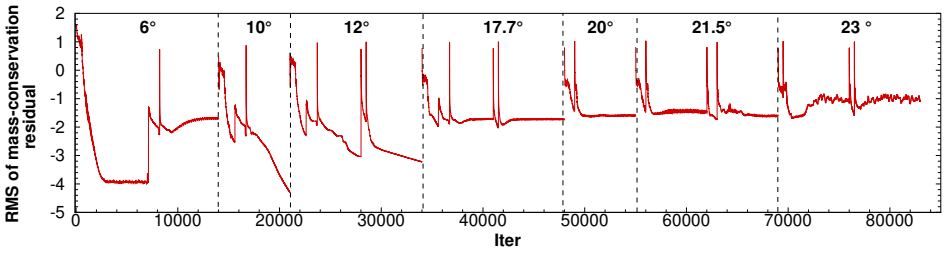

(a)

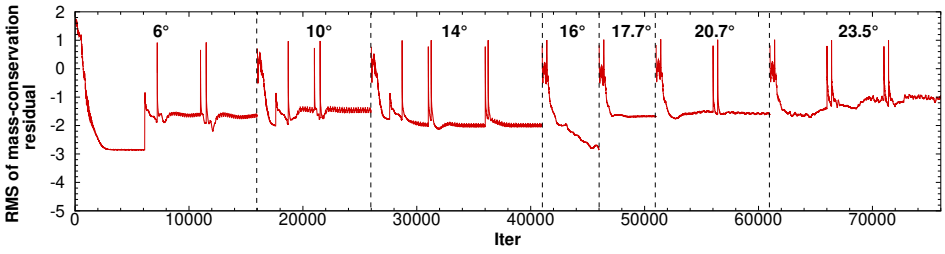

(b)

Fig. 1 Iterative convergence: RMS of mass-conservation residual for test case a) 2.2 and b) 2.3.

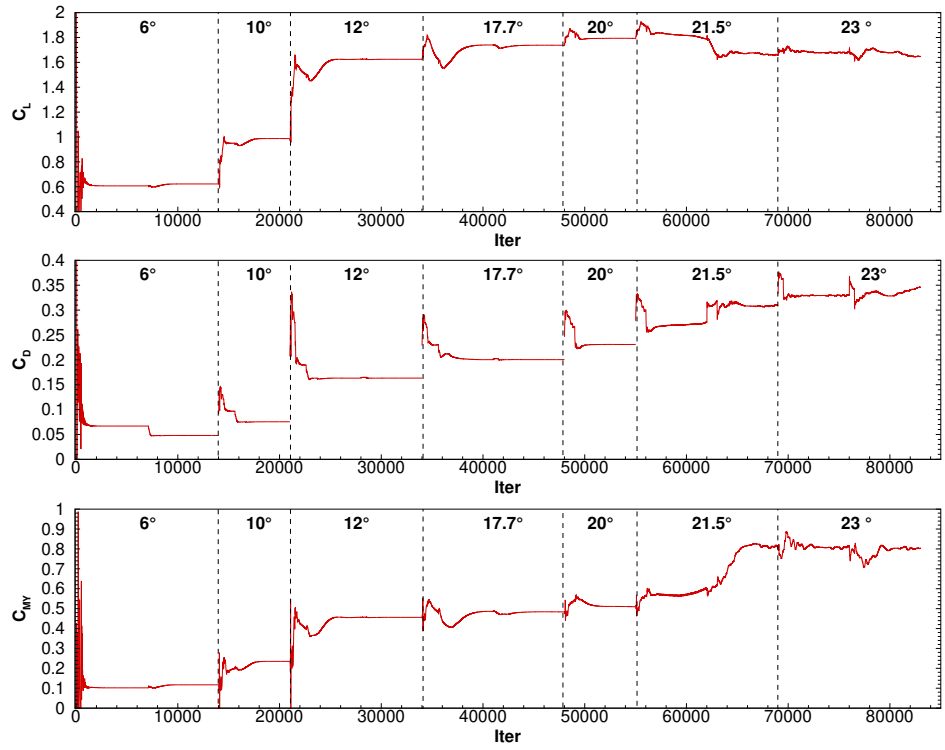

Fig. 2 Test case 2.2: iterative convergence of the aerodynamic coefficients.

number of 5.49M do not appear at all at Reynolds numbers of 30M for $\alpha = 20°$ but appear at $\alpha = 22°$. Additionally, the flow separation near the wing root also becomes narrower as the Reynolds number increases.

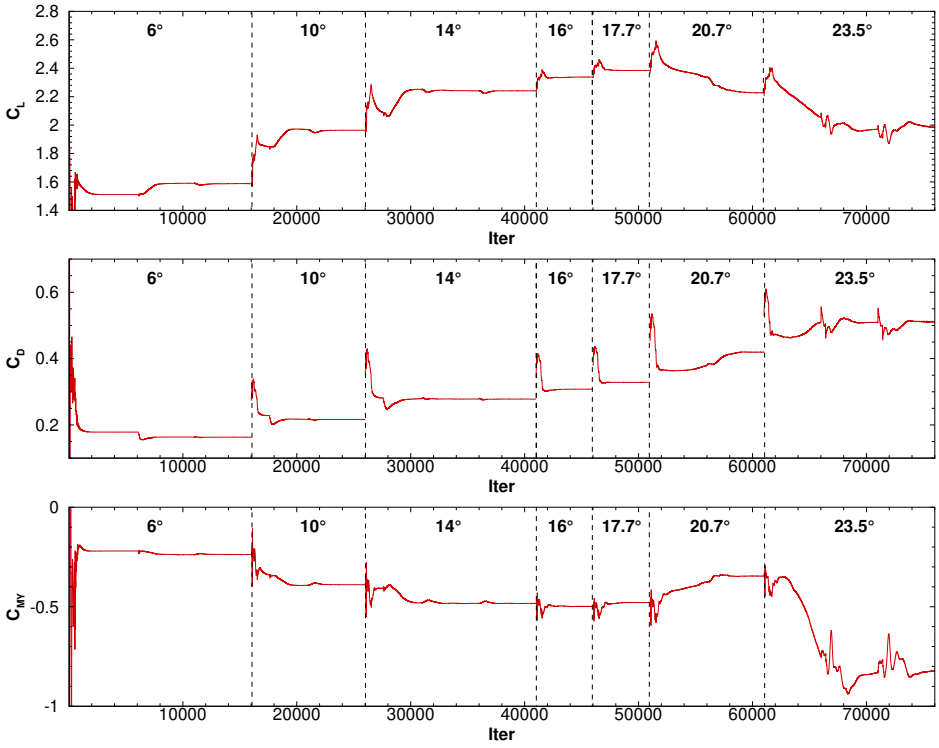

Fig. 3 Test case 2.3: iterative convergence of the aerodynamic coefficients.

C. Analysis of the results

As observed in the two last sections, when complex geometries are used for simulating high-lift configurations, RANS solvers are likely to stall and enter a limit cycle, oscillating around a mean state. This behavior is periodic and non-chaotic as seen in Fig. 9, which is of great importance for the following analysis. It is hypothesized that every RANS solution shall either converge to a steady state, in which case no modifications of the RANS solvers are required, enter a limit cycle after a sufficiently high number of iterations, or diverge. In the case of limit cycles, the periodic behavior of the pseudo-iterations process might display larger or smaller periods as shown in Fig. 9. Moreover, these limit cycles may have a simple shape or a more complex shape, meaning that the pseudo-unsteady limit cycle is caused by several pseudo-unsteady mechanisms. Here, the prefix 'pseudo' refers to the LTS strategy commonly employed by steady-state solvers, including CHAMPS, for advancing the RANS equations toward convergence.

A deeper analysis of the pseudo-unsteady and periodic mechanisms that are here highlighted is performed on a restricted amount of test cases, which is hoped to be representative of the others. To do so, test case 3.2 was selected as the primary configuration. Although several cases (2.2, 2.3, 2.4, 3.2, 3.3, and 3.4) exhibited limit-cycle behavior, the focus was placed on Case 3 configurations, as they represent the full aircraft geometry. Cases 2.2 and 2.3 were therefore excluded, along with Case 2.4, for which no RANS simulations were available for comparison with CHAMPS. Among the Case 3 configurations, Cases 3.3 and 3.4 differ from Case 3.2 only by their Reynolds number. To limit computational

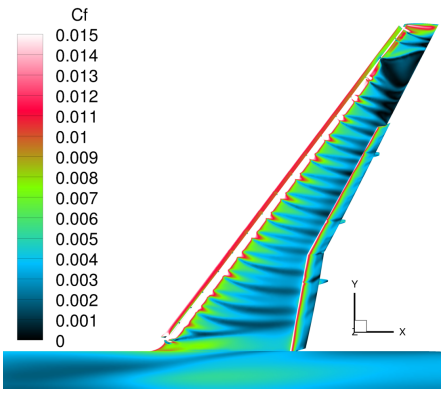

(a) $\alpha = 17.7°$**, TC2.3;**

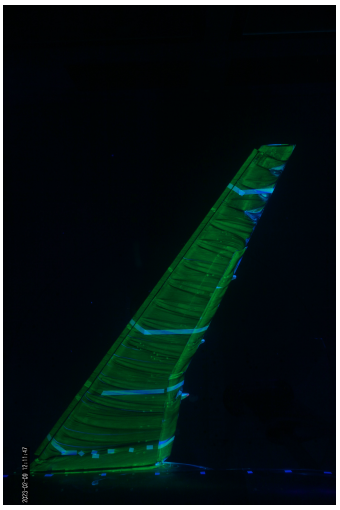

(b) $\alpha = 17.7°$**, oil-flow visualization;**

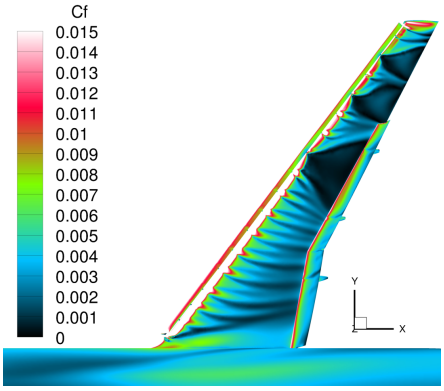

(c) $\alpha = 20.7°$**, TC2.3;**

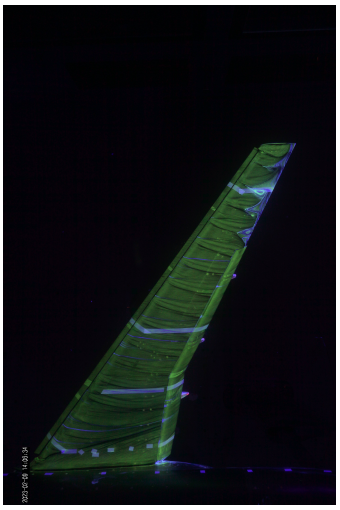

(d) $\alpha = 20.7°$**, oil-flow visualization;**

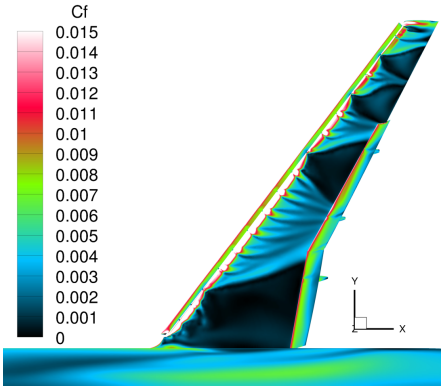

(e) $\alpha = 23.5°$**, TC2.3;**

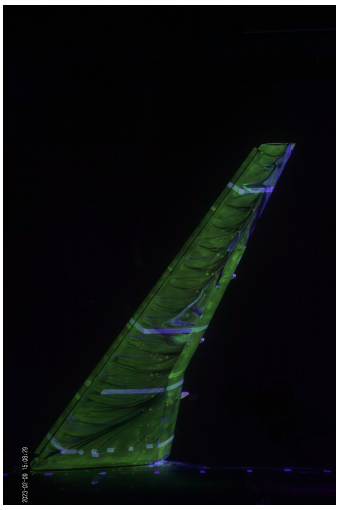

(f) $\alpha = 23.5°$**, oil-flow visualization;**

Fig. 4 Test case 2.3: separation regions development. Comparison with experimental images [3].

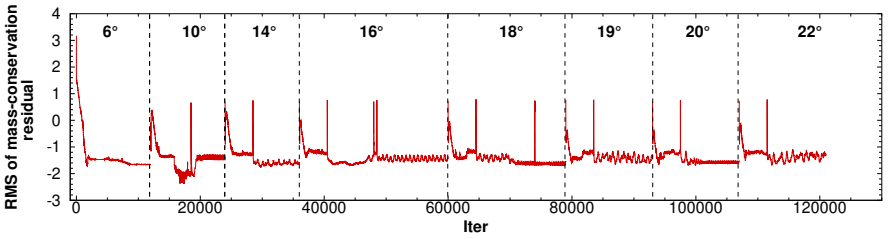

(a)

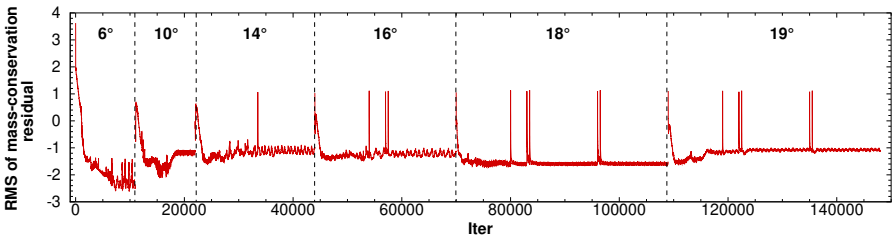

(b)

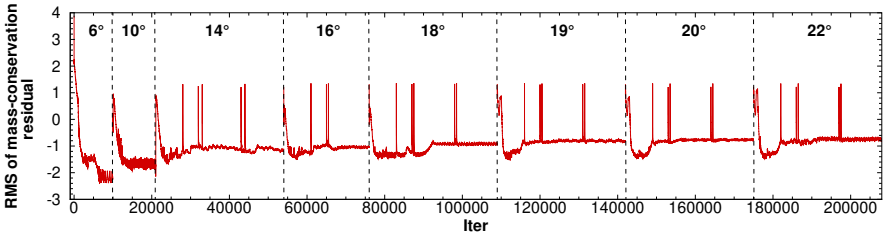

(c)

Fig. 5 Iterative convergence: RMS of mass-conservation residual for test case a) 3.2, b) 3.3, and c) 3.4.

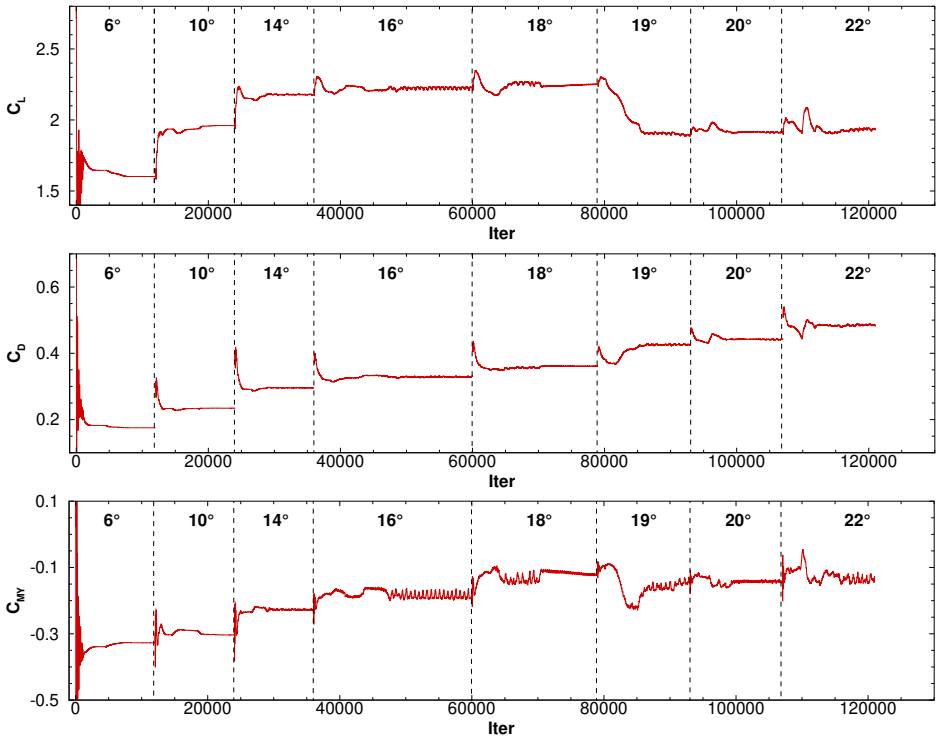

Fig. 6 Test case 3.2: iterative convergence of the aerodynamic coefficients.

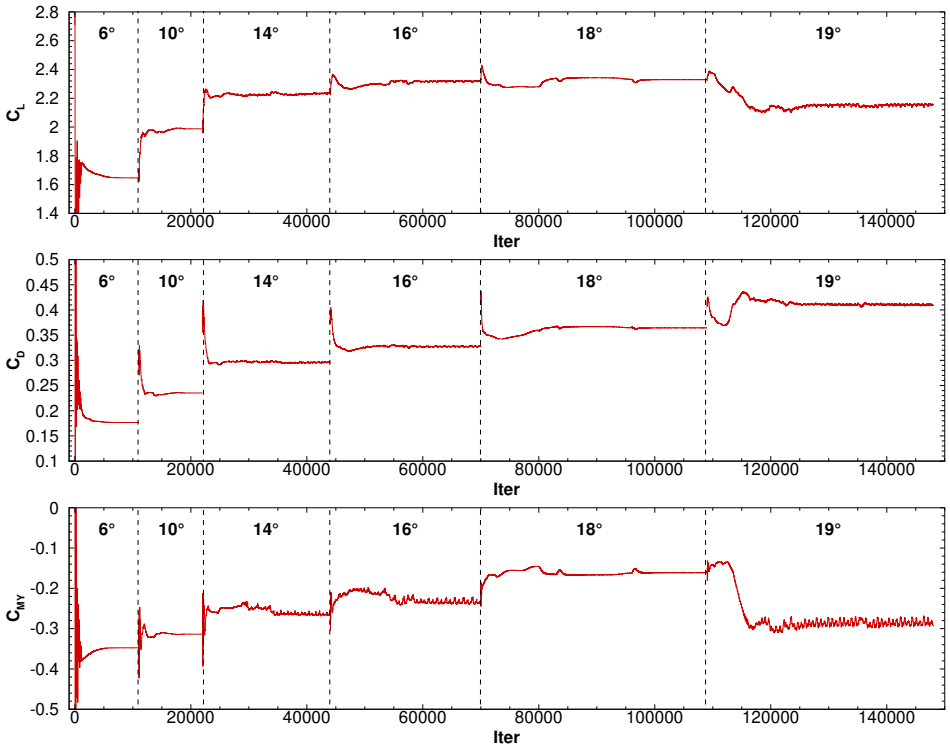

Fig. 7 Test case 3.3: iterative convergence of the aerodynamic coefficients.

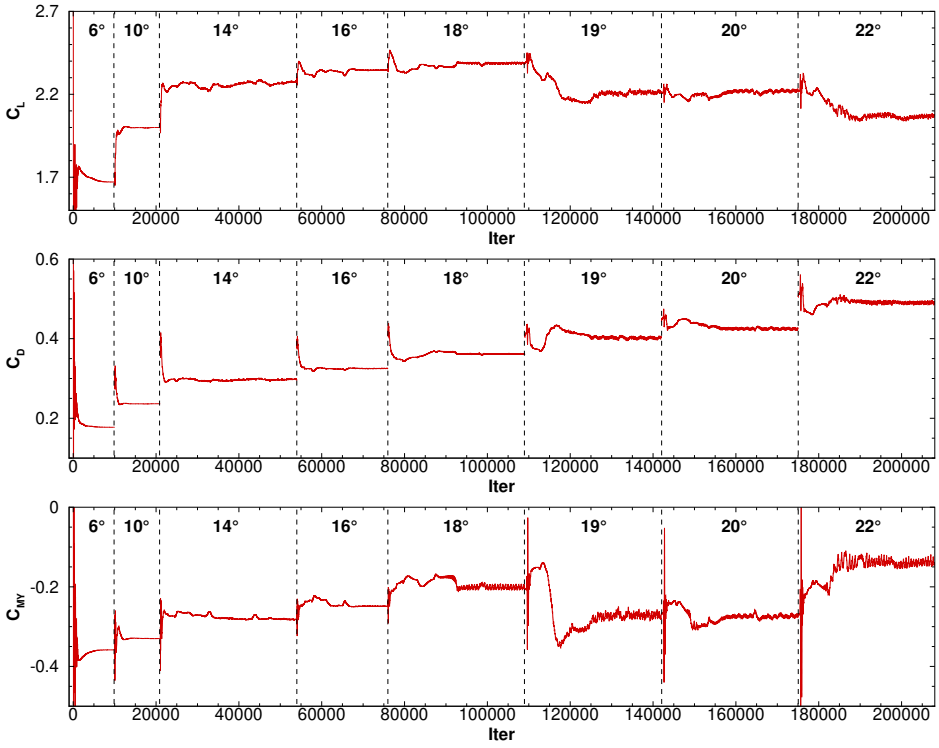

Fig. 8 Test case 3.4: iterative convergence of the aerodynamic coefficients.

cost, they were not included in the present study. The selected angles of attack—6°, 16°, and 20°—were chosen to investigate the pseudo unsteady mechanisms across different regions of the polar curve: low, moderate, and high angles. Although additional angles, particularly higher ones, could provide further insight into the method's performance, they were not investigated for the same resource-related reasons. These configurations are identified as promising avenues for future work.

From these considerations, the surface solution at 6° is analyzed. In order to extract the pseudo-unsteady mechanisms occurring in the flow, several pseudo-instantaneous surface solutions were saved within a limit cycle, whose period is shown in Fig. 10. The surface pressure coefficients are then averaged over the cycle period and subtracted from different pseudo-instantaneous surface solutions within this period. Therefore, locations on the surface of the wing that have not reached convergence and that are still changing over the iterations shall stand out from the other areas of the wing that have already reached convergence. The contours of this difference are displayed in Fig. 11 and in Fig. 12, which depicts an entire period of the limit cycle. Interestingly, only a very small part of the wing is undergoing pseudo-unsteadiness and prevents iterative convergence. Moreover, Fig. 12 clearly links the evolution of the residual value and of the lift coefficient with the fluctuating pressure coefficient values on the surface of the wing. These fluctuations take the form of vortex shedding, which is well known for preventing RANS solver iterative convergence, as, for instance, in the case of a low Reynolds flow around a cylinder.

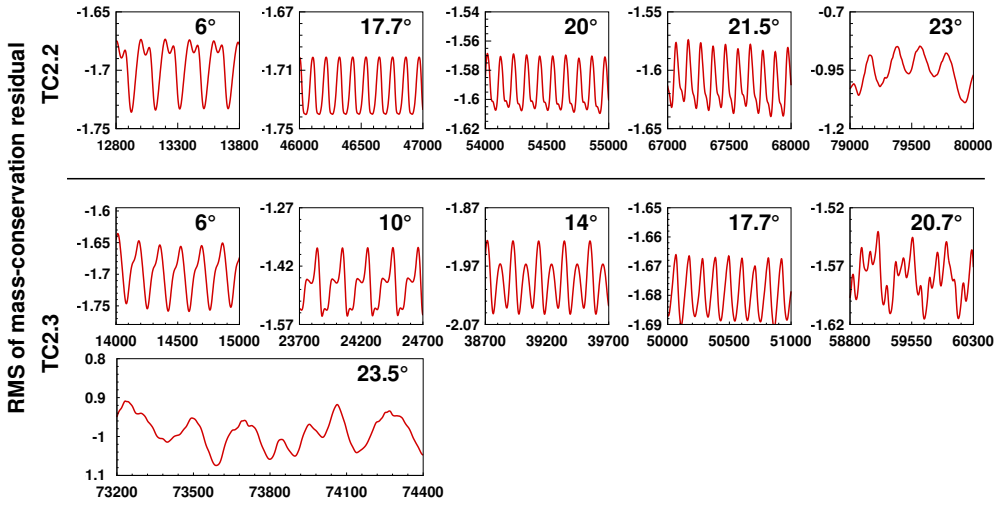

(a)

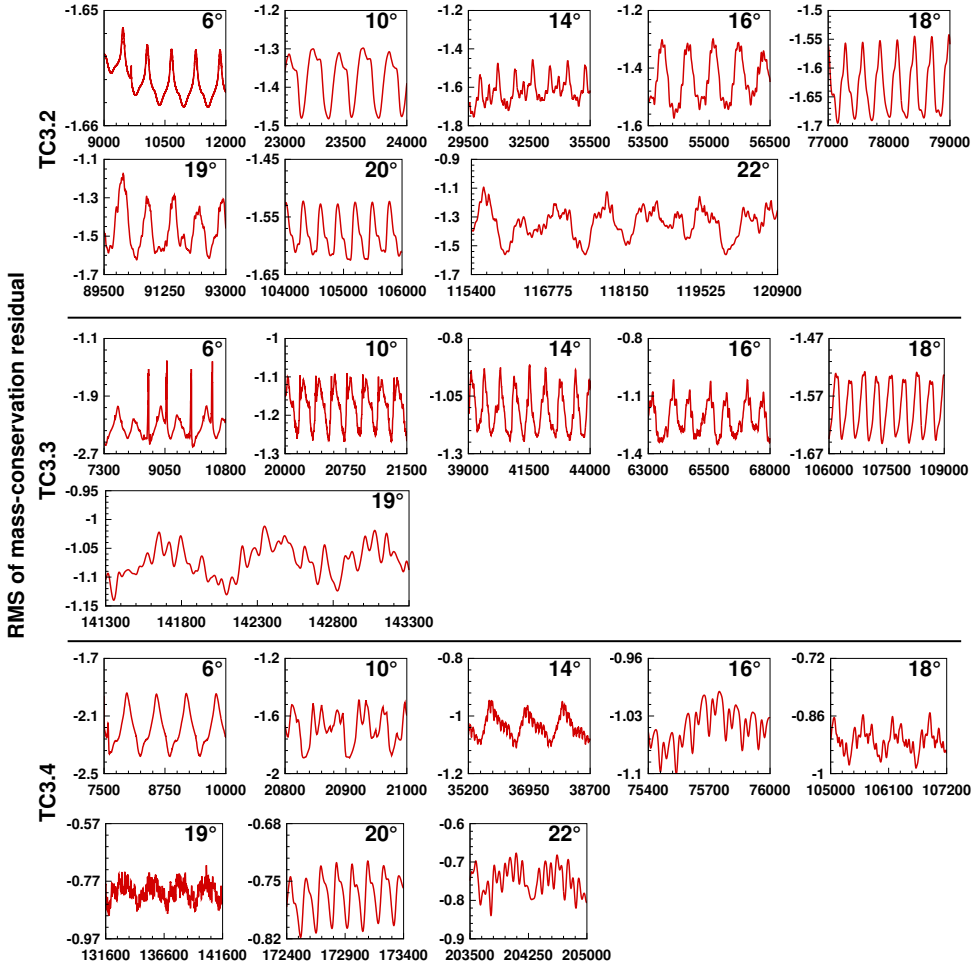

(b)

Fig. 9 Zooms on limit cycles for test case 2 and 3 at different angles of attack.

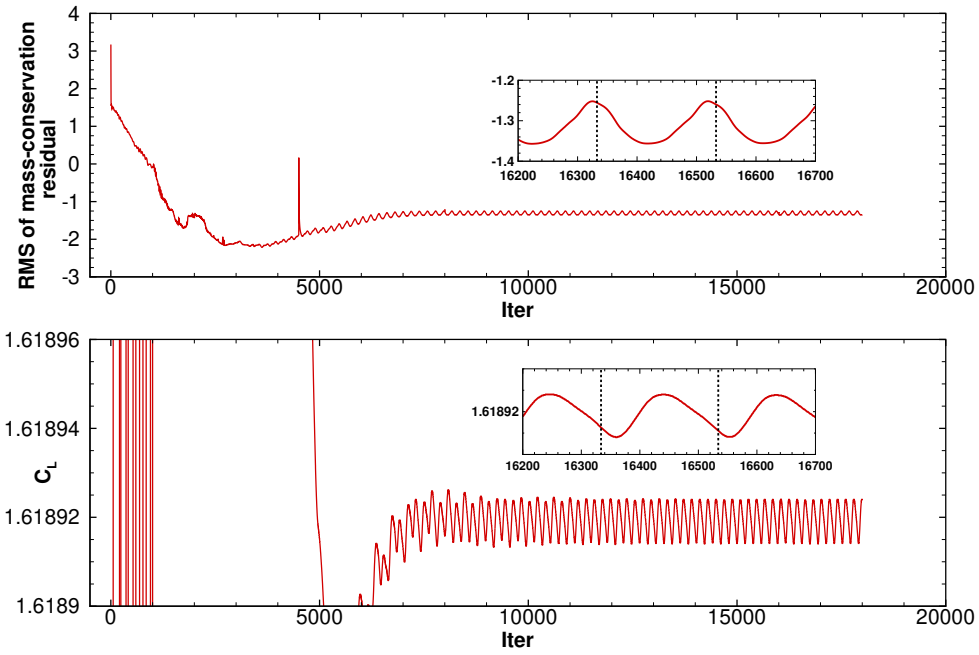

Fig. 10 Test case 3.2 at 6°: zoom on a pseudo-period in the limit cycle.

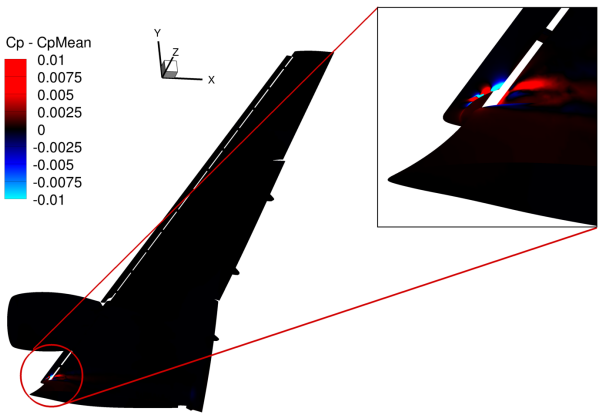

Fig. 11 Test case 3.2 at 6°: instantaneous pressure coefficient.

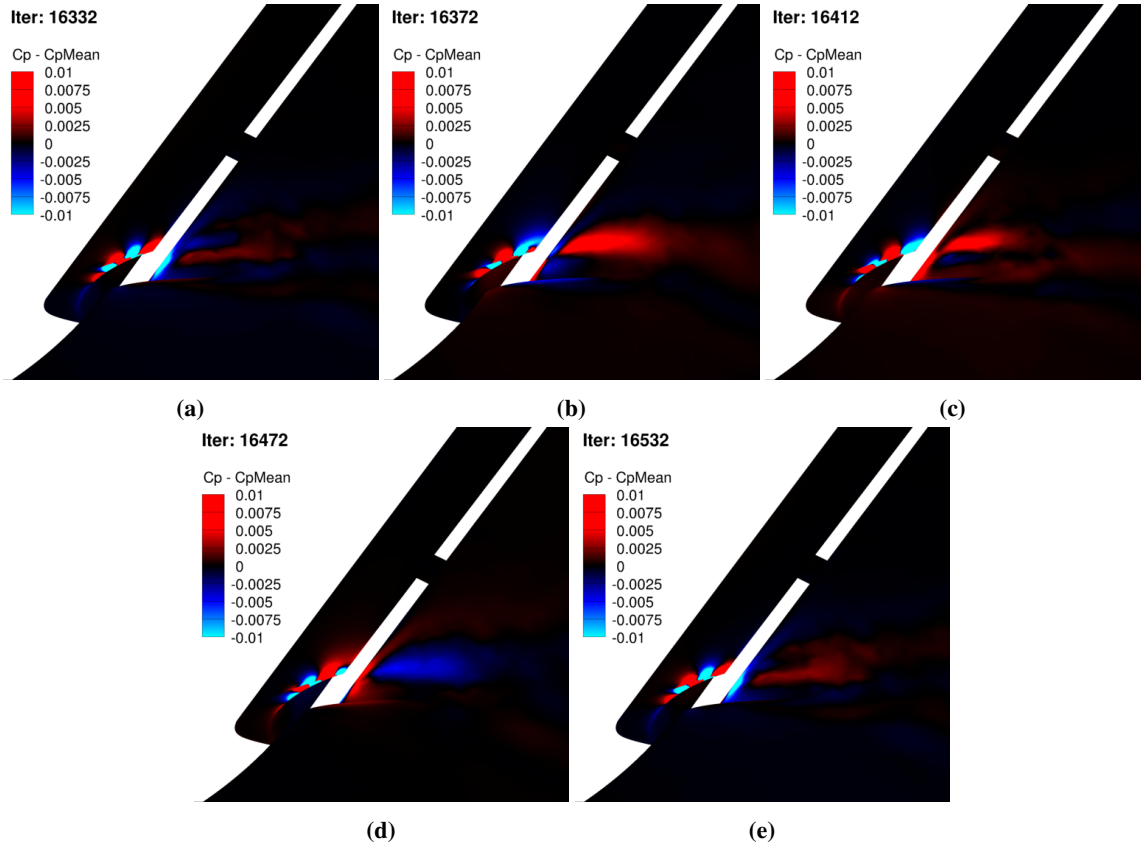

Fig. 12 Test case 3.2 at $\alpha = 6°$: pseudo-instability over a pseudo-period, successively at iterations a) 16332, b) 16372, c) 16412, d) 16472, and e) 16532.

As these observations efficiently underlined the nature of the pseudo-unsteadiness for this test case, similar manipulations are done for Test Case 3.2 at 16°. The iterative convergence for this case is displayed in Fig. 13. As already observed above, the residual convergence displays a pseudo-periodic behavior. In the same manner as for the case at 6°, a specific period can be isolated and studied.

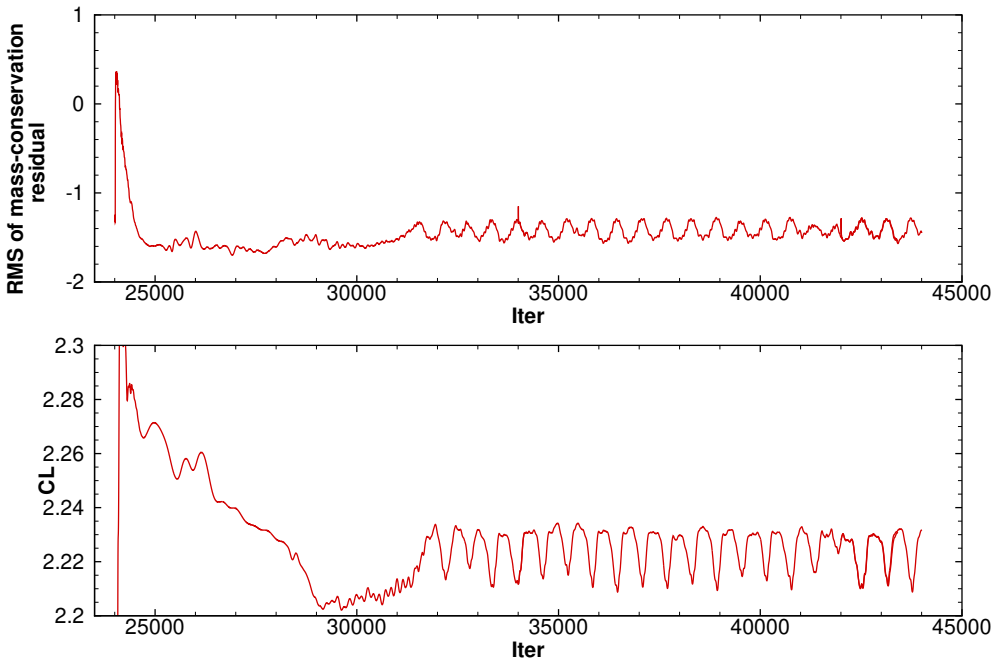

Fig. 13 Test case 3.2 at 16°: zoom on a pseudo-period in the limit cycle.

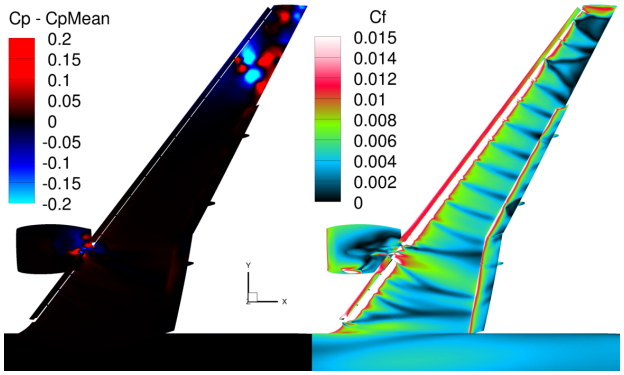

Fig. 14 Test case 3.2 at 16°: instantaneous pressure coefficient and skin friction.

The surface contours of the fluctuating surface pressure coefficient are presented in Fig. 14 and 15. The pseudo-unsteady region located on the inboard slat from the previous case did not develop for this case. More interestingly, the development of a pseudo-unsteady region emerging from the outboard slat brackets corresponds to the regions where the pizza-slice structure developed. These structures display an alternating pattern of higher and lower pressure peaks, similar to what is encountered in the wake of a cylinder when vortex shedding occurs. This observation informs us of

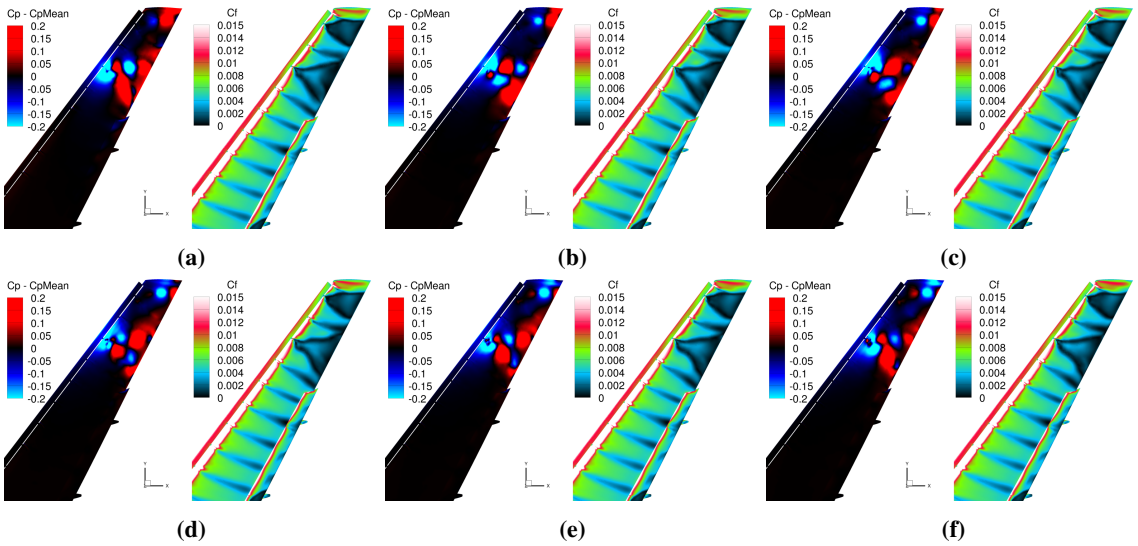

Fig. 15 Test case 3.2 at $\alpha = 16°$: pseudo-instability over a pseudo-period, successively at iterations a) 39540, b) 39661, c) 39782, d) 39902, e) 40023, and f) 40144.

the nature of the spurious separations observed in RANS solutions. Similarly, shedding emerges from the outermost brackets at the tip of the wing, displaying similar patterns of alternating high and low peaks of pressure, akin to vortex shedding. Additionally, some pseudo-unsteadiness appears around the nacelle and are displayed in Fig. 16a and Fig. 16b.

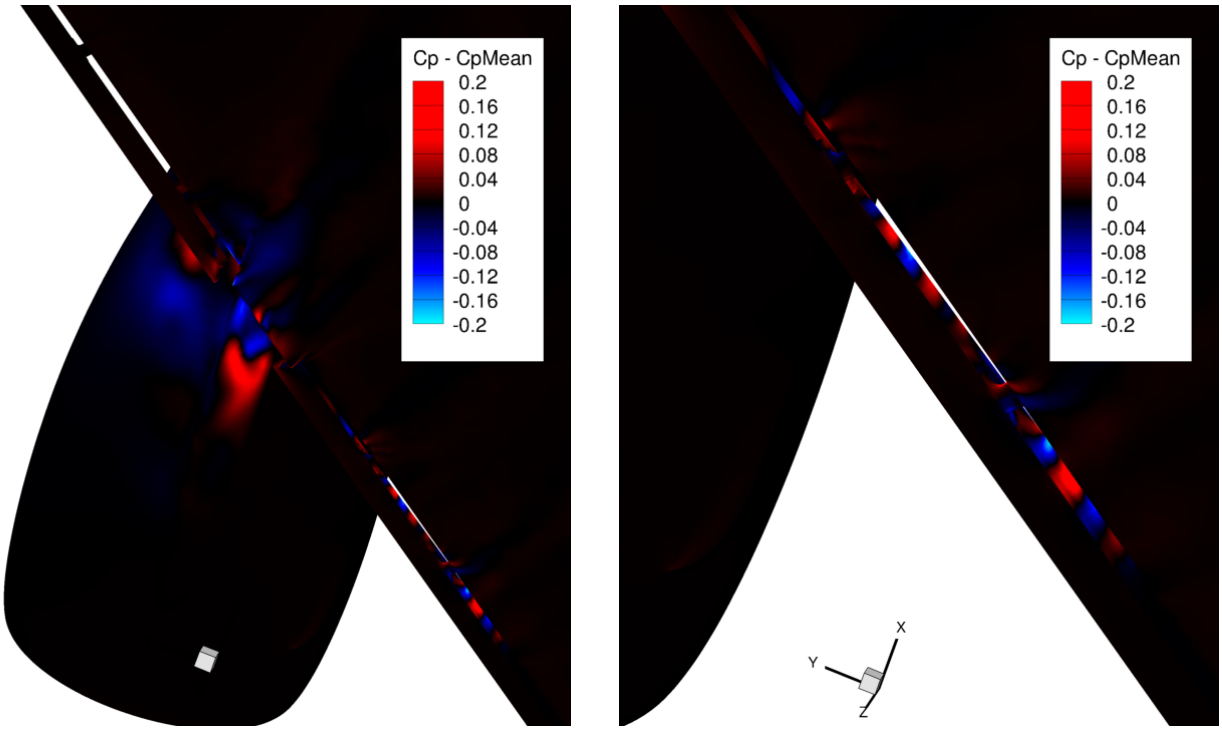

(a) Engine. **(b) Slat.**

Fig. 16 Test case 3.2 at 16°: instantaneous pressure coefficient distributions.

Similar manipulations were performed for the same configuration at 20°, for which the iterative convergence is displayed in Fig. 17. Here again, the residual convergence displays a pseudo-periodic behavior, in the same manner as for the cases at 6° and 16°. Therefore, this pseudo-period is isolated and studied in the same manner as the one used for the two previous angles of attack. An instantaneous snapshot of the skin friction coefficient alongside the fluctuating pressure coefficients is displayed in Fig. 18. Figure 19 highlights the periodic evolution of the pseudo-unsteady mechanism occurring in the wake of the most outboard slat brackets.

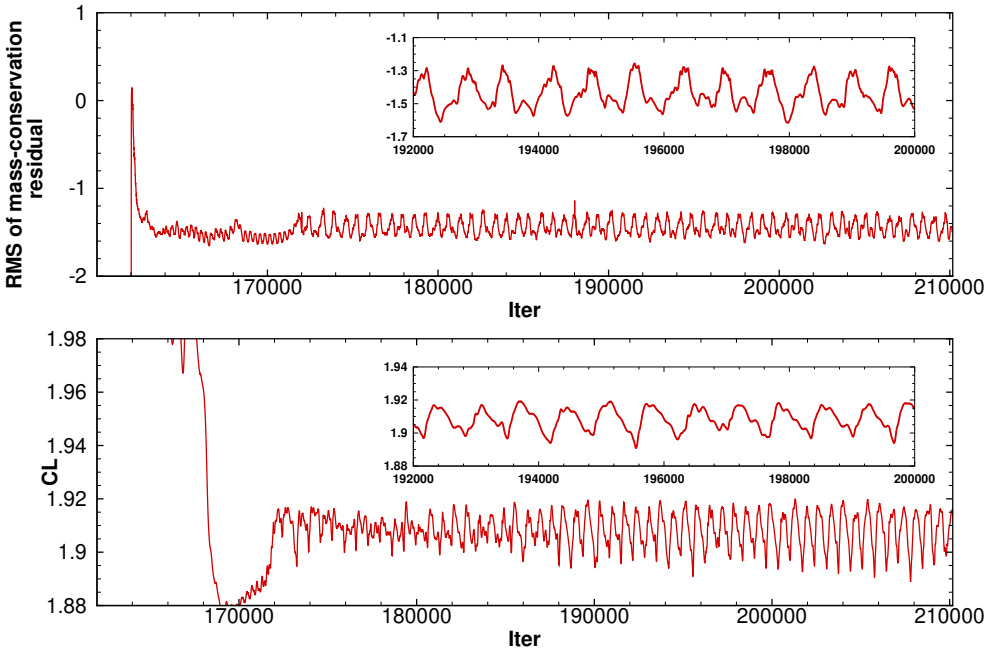

Fig. 17 Test case 3.2 at 20°: zoom on a pseudo-period in the limit cycle.

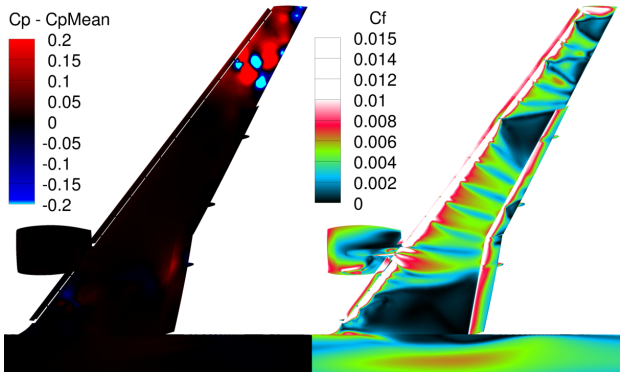

Fig. 18 Test case 3.2 at 20°: instantaneous pressure coefficient and skin friction.

For all the above analyses, it is crucial to emphasize that the observed features should be interpreted as resembling unsteady flow phenomena rather than definitively identifying them as such. This caution arises because these results are obtained via a LTS method, which does not provide time-accurate solutions, even though local time steps might

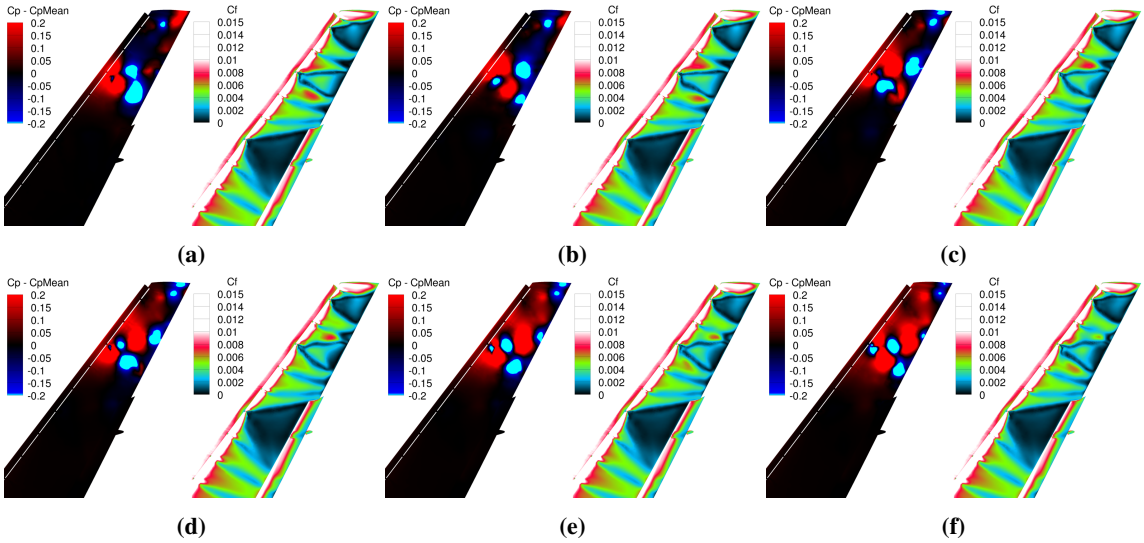

Fig. 19 Test case 3.2 at $\alpha = 20°$: pseudo-instability over a pseudo-period, successively at iterations a) 197645, b) 197784, c) 197922, d) 198060, e) 198200, and f) 198339.

be of similar amplitude in limited regions of the flow. Although these observations are very likely linked to unsteady physics, only fully URANS simulations can conclusively confirm the true nature of these pseudo-unsteady observations. Therefore, these findings primarily reflect the characteristics of the pseudo-unsteadiness captured by the solver during the iterative process toward a steady state, rather than direct evidence of genuine unsteady flow phenomena.

In summary, the above analyses reveal that the residuals consistently enter periodic limit cycles at specific frequencies, each associated with one or more pseudo-unsteady mechanisms. Based on this observation, it is hypothesized that a method capable of enforcing convergence in a simplified case—characterized by a single pseudo-periodic mechanism—should remain effective in more complex scenarios involving multiple such mechanisms. This hypothesis is grounded in the idea that complex unsteady behaviors can often be understood as combinations of simpler ones. Knowing that in many cases, the instability encountered for high-lift configurations is the combination of multiple pseudo-unsteady phenomena—similar to what could be called pseudo vortex sheddings, which display a pseudo-periodic behavior—is of great importance. Indeed, a method called Selective Frequency Damping has been developed in the literature to specifically tackle these situations and can then be applied to stabilize such simulations. This method is presented in the next section.

IV. Selective Frequency Damping

A. Literature

Selective Frequency Damping (SFD) [12] is a mathematical approach designed to be integrated into existing solvers to suppress undesired oscillations. It operates under the assumption that the system possesses a steady-state solution,

which can be reached if an unsteady mode preventing convergence is effectively damped. The method was initially introduced by Åkervik et al. [12] in its original coupled formulation.

The detailed mathematical formulation and developments are presented in subsequent sections of this document. However, a brief overview of Åkervik's pioneering work [12] is relevant here. The authors demonstrated the effectiveness of SFD by successfully stabilizing a Direct Numerical Simulation (DNS) for a bidimensional flow over a long cavity. Since then, this technique has been employed by numerous researchers for various applications, including jet in crossflow [13], lifted flame [14, 15], sphere wake [16], and thin aerofoil wake [17]. More recently, Moise [18] used SFD to achieve a steady solution for a bubble vortex breakdown in a laminar swirling jet.

An important advancement of the original method was introduced by Jordi et al. [19] through the Encapsulated Selective Frequency Damping (ESFD) formulation. This alternative implementation was motivated by the significant modifications required for the original SFD approach, which involved adding a source term and solving an augmented set of equations. ESFD mitigates these challenges by decoupling the original solver from the low-pass time-filtered flow computation and source term correction, simplifying its integration into existing solvers.

ESFD has been successfully applied in various studies as for instance, Casacuberta et al. [20] stabilized vortex shedding from a cylinder using DNS, while Plante et al. [21] addressed tridimensional buffet over a wing using RANS. Further examples include stabilization of shear-driven cavity flow by Bengana et al. [22], natural circulation systems by Pini et al. [23], and laminar separation bubbles by Rodriguez et al. [24].

Recent research has also explored alternative implementations of SFD. Plante and Laurendeau [25] proposed a local selection of the Δ parameter to damp numerical oscillations, thereby enhancing the convergence rate of RANS-based steady-state solvers. Paladini et al. [26] developed another variant by selectively applying the stabilizing source term to specific regions of the computational domain, enabling targeted stabilization to suppress unsteady phenomena. This approach was tested successfully on transonic buffet over an airfoil using URANS.

This study aims to expand the understanding and adoption of SFD within the CFD community by demonstrating its effectiveness in achieving deeply converged solutions for high-lift configurations involving complex three-dimensional geometries. To the author's knowledge, only Zauner et al. [27] have recently attempted to apply the SFD method for enforcing convergence in high-lift configurations using RANS simulations. Their findings indicate that while SFD reduces the oscillation amplitudes of aerodynamic coefficients, it does not help to achieve machine-precision convergence. Additionally, their work does not include iterative convergence plots; instead, it only reports the mean aerodynamic coefficients and an extended root mean square (RMS) definition for drag, lift, and pitching moment as convergence measures. Furthermore, no detailed analysis of SFD's effects on steady RANS simulations is provided within their contribution.

B. Theorical formulation

Consider a nonlinear dynamical system with appropriate initial and boundary conditions for the vector quantity $\boldsymbol{q}$ under the operator $\boldsymbol{f}$. For a flow problem, such a system can be the RANS equations and is given by:

$$\dot{\boldsymbol{q}} = \boldsymbol{f}(\boldsymbol{q}) \tag{1}$$

where the $(\dot{})$ is used to denote the derivative with respect to time, $\boldsymbol{q}$ are the conservative variables, and $\boldsymbol{f}$ represents the summation of the convective fluxes, the viscous fluxes, and the source terms if there are any. Under the assumption that a steady-state solution exists for this system of equations, this solution of the system is denoted $\boldsymbol{q_s}$ and fulfills:

$$\dot{\boldsymbol{q}}_{\boldsymbol{s}} = \boldsymbol{f}(\boldsymbol{q}_{\boldsymbol{s}}) = \boldsymbol{0} \tag{2}$$

Now, if the considered solution is unstable, any perturbed flow state, or any state close but not equal to $\boldsymbol{q_s}$, will quickly depart from $\boldsymbol{q_s}$. In order to stabilize such system, Akervik et al. [12] proposed a regularization method based on a proportional feedback control. For such, the error between the desired state (here the unstable but steady-state solution $\boldsymbol{q_s}$) and the actual state is denoted $\boldsymbol{e}$ and reads:

$$\boldsymbol{e}(t) = \boldsymbol{q}_{\boldsymbol{s}}(t) - \boldsymbol{q}(t) \tag{3}$$

To implement this control, the dynamic system described in Eq. (1) is modified by adding a control term proportional to this error:

$$\dot{\boldsymbol{q}} = \boldsymbol{f}(\boldsymbol{q}) - \chi \left(\boldsymbol{q}(t) - \boldsymbol{q}_{\boldsymbol{s}}(t)\right) \tag{4}$$

where χ is the control coefficient of the controller. In this initial form, the target solution of the controller is the steady-state solution $\boldsymbol{q_s}$ which is not known a priori. Therefore, this term is replaced by a modification of $\boldsymbol{q}$ with reduced temporal fluctuations, which takes the form of a temporally low-pass filtered solution $\overline{\boldsymbol{q}} = \boldsymbol{T} * \boldsymbol{q}$, which is the convolution of $\boldsymbol{q}$ with a temporal filter kernel $\boldsymbol{T}$. The modified equation then reads:

$$\dot{\boldsymbol{q}} = \boldsymbol{f}(\boldsymbol{q}) - \chi \left(\boldsymbol{q}(t) - \overline{\boldsymbol{q}}(t)\right) \tag{5}$$

Here, it is important to note that as $\boldsymbol{q}$ is approaching the steady state $\boldsymbol{q_s}$, the filtered solution will in turn approach $\boldsymbol{q_s}$, therefore reducing the influence of the applied controller until the steady state is reached at which point $\overline{\boldsymbol{q}}$ gets identical to $\boldsymbol{q} = \boldsymbol{q_s}$. Thus, the steady-state solution of the modified dynamic system in Eq. (5) is also a solution of the initial dynamic system in Eq. (1). In other words, there is no generation of an additional solution if the numerical solver

reaches convergence.

Moreover, from Akervik et al. [12], the causal low-pass time-filter uses the exponential kernel and takes the form:

$$\overline{\boldsymbol{q}}(t) = \int_{-\infty}^{t} \frac{1}{\Delta} exp(\frac{\tau - t}{\Delta}) \boldsymbol{q}(\tau) d\tau \tag{6}$$

with $\overline{\boldsymbol{q}}$ the temporally filtered flow state, and Δ the filter width associated with the cutoff frequency $\omega_c = 1/\Delta$. For engineering applications, the integral formulation of the filter is impractical as it would require the storage of the entire time history of $\boldsymbol{q}$. Therefore, the equivalent differential form of this equation was advised by Akervik et al. :

$$\dot{\overline{\boldsymbol{q}}}(t) = \frac{\boldsymbol{q}(t) - \overline{\boldsymbol{q}}(t)}{\Delta} \tag{7}$$

which can be advanced in time using integration schemes. The final version of the system in Eq. (1) is then expressed as:

$$\begin{cases} \dot{\boldsymbol{q}} = \boldsymbol{f}(\boldsymbol{q}) - \chi \left(\boldsymbol{q}(t) - \overline{\boldsymbol{q}}(t) \right) \\ \dot{\overline{\boldsymbol{q}}} = \dfrac{\boldsymbol{q} - \overline{\boldsymbol{q}}}{\Delta} \end{cases} \tag{8}$$

A significant challenge of this formulation lies in the potentially extensive modifications required for implementation into an existing RANS solver. To mitigate this difficulty, Jordi et al. [19] proposed an encapsulated approach using a sequential operator-splitting method. This approach divides the augmented set of equations into two sub-problems, solved iteratively. The second sub-problem uses the iterated result of the first as its initial condition. The first sub-problem involves solving the RANS equations using the baseline solver:

$$\begin{pmatrix} \dot{\boldsymbol{q}} \\ \dot{\overline{\boldsymbol{q}}} \end{pmatrix} = \begin{pmatrix} \boldsymbol{f}(\boldsymbol{q}) \\ \boldsymbol{0} \end{pmatrix} \tag{9}$$

As such, the time iteration for the first sub-problem can be presented as a time iteration of the solver, represented by the $\boldsymbol{\Psi}$ operator:

$$\begin{pmatrix} \boldsymbol{q}^{n+0.5} \\ \overline{\boldsymbol{q}}^{n+0.5} \end{pmatrix} = \begin{pmatrix} \boldsymbol{\Psi}(\boldsymbol{q}^{n}) \\ \overline{\boldsymbol{q}}^{n} \end{pmatrix} \tag{10}$$

The second sub-problem includes the effect of the additional source term and the calculation of the low-pass time-filtered version of the flow.

$$\begin{pmatrix} \dot{\boldsymbol{q}} \\ \dot{\overline{\boldsymbol{q}}} \end{pmatrix} = \begin{pmatrix} -\chi \boldsymbol{I} & \chi \boldsymbol{I} \\ \frac{\boldsymbol{I}}{\Delta} & -\frac{\boldsymbol{I}}{\Delta} \end{pmatrix} \begin{pmatrix} \boldsymbol{q} \\ \overline{\boldsymbol{q}} \end{pmatrix} \tag{11}$$

which is a linear differential equation whose exact solution is:

$$\begin{pmatrix} \boldsymbol{q}^{n+1} \\ \overline{\boldsymbol{q}}^{n+1} \end{pmatrix} = \frac{1}{1+\chi\Delta} \begin{pmatrix} \boldsymbol{I} + \chi\Delta \boldsymbol{I} e^{-(\chi+\frac{1}{\Delta})\Delta t} & \chi\Delta \boldsymbol{I} \left(1 - e^{-(\chi+\frac{1}{\Delta})\Delta t}\right) \\ \boldsymbol{I} - \boldsymbol{I} e^{-(\chi+\frac{1}{\Delta})\Delta t} & \chi\Delta \boldsymbol{I} + \boldsymbol{I} e^{-(\chi+\frac{1}{\Delta})\Delta t} \end{pmatrix} \begin{pmatrix} \boldsymbol{q}^{n+0.5} \\ \overline{\boldsymbol{q}}^{n+0.5} \end{pmatrix} \tag{12}$$

This segregated formulation — using Eq. 10, and then Eq. 12 — enables the original solver to be employed with minimal modifications.

As seen above, the classical SFD approach relies on a single set of control parameters, applied uniformly across the entire computational domain and to all governing equations, which is the case in this work. This choice implicitly assumes that the dominant instability is global in nature, or at least that the flow dynamics are governed by a single, well-defined frequency. However, such an assumption may not always hold. The unstable mode can be spatially localized—such as in the case of shock buffet instabilities—or multiple distinct instabilities with different spatial supports and frequencies may coexist within the flow. Nevertheless, this does not necessarily undermine the applicability of the SFD method. One must recall that SFD acts as a temporal low-pass filter, which means that selecting a cut-off frequency $\omega_c = 1/\Delta$ tailored to the lowest-frequency instability ensures that all higher-frequency modes are also damped. The main limitation of this global approach is not its ability to damp instabilities, but rather its efficiency in driving the flow toward a steady-state solution. Since the filtering is applied uniformly, regions may be over-damped unnecessarily, potentially slowing the overall convergence process. A spatially varying approach could, in theory, improve efficiency by applying SFD only where needed. Work done by Plante and Laurendeau [25] tackles such question by replacing the filter width Δ by the local time-step value, showing an improved convergence rate on a RANS case of the RAE2822 airfoil in transonic regime. Pursuing a similar objective, Paladini et al. [26] developed a variant of the method in which the stabilizing source term is applied selectively to specific regions of the computational domain. This localized treatment enables more efficient suppression of pseudo-unsteady behaviors by concentrating the damping effect in the areas where it is most effective.

Another important aspect to consider is the impact of applying LTS in conjunction with SFD- as done in this work-, which was initially developed for unsteady flows using time-accurate methods (see, e.g., [12]). While several studies (e.g., [25, 28]) have demonstrated the effectiveness of SFD in accelerating convergence toward steady-state solutions even when used with LTS, this combination raises questions about the interpretation of the SFD parameters. Indeed, when LTS is employed, time no longer evolves uniformly throughout the domain. Consequently, parameters such as χ and Δ lose their direct connection to physical time scales and instead relate to the solver's local advancement of time.

More precisely, this means that the filtering operation governed by Eq. (12) is no longer applied homogeneously across the domain, as the time step Δt is effectively replaced by a local value Δt_i for each cell i. Therefore, in regard to the previous discussion on global SFD parameters, a more relevant approach to understanding the behavior of SFD under LTS would be to consider the coupling between the local SFD parameters and the local-time step—namely, through the products $\chi_i \Delta t_i$ and $\Delta t_i / \Delta_i$ in Eq. (12), which is out of the scope of this work.

In this study, the selection of the SFD control parameters is based on visual inspection of the unstable solution, which generally provides a sufficient first estimate for χ and Δ. More specifically, following the approach of Åkervik et al.[12], the parameters χ and Δ are estimated from the dominant oscillation period T observed during the iterative process—typically visible in the lift coefficient—and are set to $\chi = 1/(2T)$, and $\Delta = 2T$. No further optimization of the SFD parameters was performed, as the selected values already provided a substantial improvement in iterative convergence—fulfilling the primary objective of this study. A more in-depth investigation would be required to fully characterize the influence of each parameter on convergence behavior. Yet, it remains an open question regarding how to select the optimal parameter set for the SFD method apriori. Study by Liguori [28] tackle this subject while works by Jordi et al. [29], Cunha et al. [30], and Casacuberta et al. [20] propose plausible methods for automatically choosing and adapting these parameters during a simulation, but this has yet to be implemented in CHAMPS.

Finally, it can be seen that from the integral formulation of the time-filter in Eq. (6), which is equivalent from the one in Eq. (7), that the low-pass time-filtered solution $\overline{\boldsymbol{q}}$ is influenced by all the past iterations of the flow calculated by the solver. This can be problematic since as the convergence of the solver increases, the iterations that are further back in time tend to skew the result of the filter away from the actual solution toward which the solver converges in the most recent iterations. This will result in an increased computational time due to slow convergence rate. However, as proposed in [28], the convergence can be accelerated by periodically resetting the time-filtered solution to the current flow field after every r iterations. This effectively re-initializes the filter with what is hoped to be a more accurate approximation of the partially converged solution. The resulting algorithm remains the same as the one presented above, with the only difference being that for the m^{th} iteration, where m is a multiple of r, an additional step is done at the end of the iteration:

$$\begin{pmatrix} \boldsymbol{q}^{m+1} \\ \overline{\boldsymbol{q}}^{m+1} \end{pmatrix} = \begin{pmatrix} \boldsymbol{q}^{m+1} \\ \boldsymbol{q}^{m+1} \end{pmatrix} \quad , \quad m \in \{kr \mid k \in \mathbb{N}^*\} \tag{13}$$

In this work, the reset parameter is then arbitrarily chosen to be larger than Δ, based on prior experience, which proved sufficient to ensure convergence. A more comprehensive analysis of its influence is available in Liguori et al. [28], where the impact of different reset values is assessed in two-dimensional test cases. Thus, SFD requires the user to set up three parameters, which are χ the control coefficient of the controller, Δ the width of the time filter and r, the number

of iterations between every reset of the filtered flow.

C. Numerical results

For all results presented in this work the Courant–Friedrichs–Lewy (CFL) number was set to a value of 10^5, and 10 BSGS sweeps were performed at each iterations to solve the linear system.

To assess the effectiveness of the SFD method, Test Case 3.2 was selected as the primary configuration for the same reasons that were already highlighted in Sec. III.C . The selected angles of attack—6°, 16°, and 20°—were chosen to evaluate the performance of the SFD method across different regions of the polar curve: low, moderate, and high angles.

Employing the SFD method for the three configurations yielded very successful results in terms of iterative convergence. For each test case, deep convergence was achieved (see Fig. 20, 21, and 22). For conciseness, only the root-mean-square of the continuity-equation residual is reported in this work; however, all residuals exhibit a similar convergence behavior.

The set of parameters used for each case is summarized in Table 1. The different convergence rates observed in the iterative convergence plots in Fig. 20 reveal the effect of using different parameter combinations. The different parameter sets tested for the case at 6° clearly shows that under a poor selection of these parameters, the convergence is slowed, whereas a relevant selection of these parameters leads to accelerated convergence. As the χ parameter represents the proportional gain of the additional proportional controller source term, it can be interpreted as a damping factor. The reason for the increase of its value during the case at 6° is that a more aggressive damping was sought to improve the converging rate of the iterative solver, which indeed improved it as seen in Fig. 20. Although accelerated convergence was obtained here for all tested cases, a parameter sensitivity study would help identify the optimal set of parameters for these cases.

Table 1 Test case 3.2: SFD parameters

Angle of attack	χ	Δ	r
6° from Iter 8000 to 16000	$2.577 \cdot 10^{-3}$	388	500
6° from Iter 16000 to 34000	$2.577 \cdot 10^{-2}$	388	500
16°	$8.197 \cdot 10^{-4}$	1220	4500
20°	$7.246 \cdot 10^{-4}$	1380	7500

One may also have noticed that when applying the SFD method and reaching a steady-state solution, the converged aerodynamic coefficients do not correspond to the mean value of the aerodynamic coefficients observed during the limit cycle phase. This difference is even more noticeable in the iterative convergence plots of the drag and pitching moment coefficients in Fig. B1, B2, and B3 in Appendix. The comparison is summarized in Table 2. In fact, this observation is not surprising. Let's consider, for instance, a converged steady-state solution. If this solution is perturbed from its

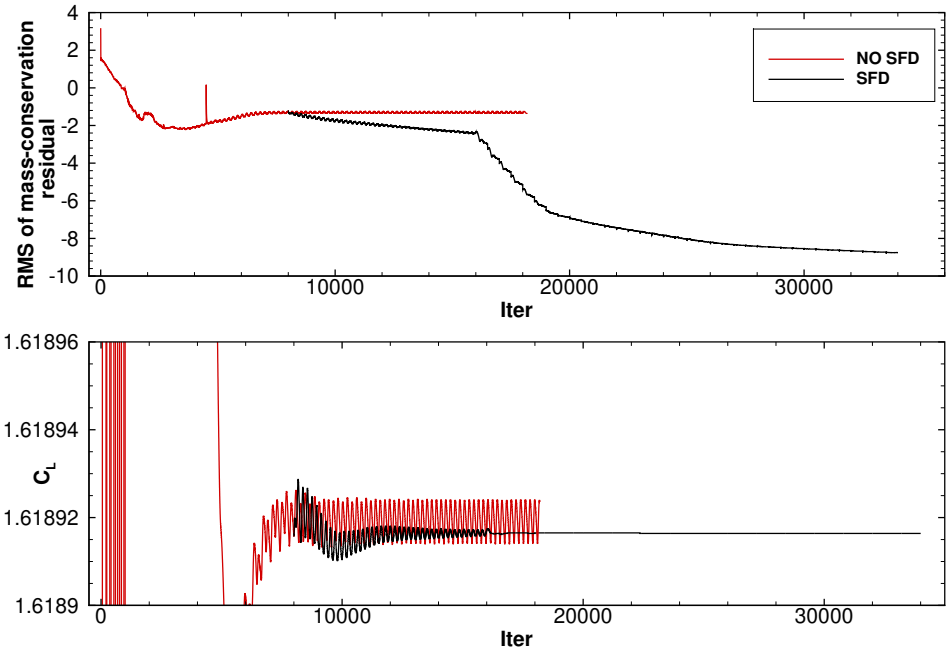

Fig. 20 Test case 3.2 at $\alpha = 6°$: iterative convergence using SFD.

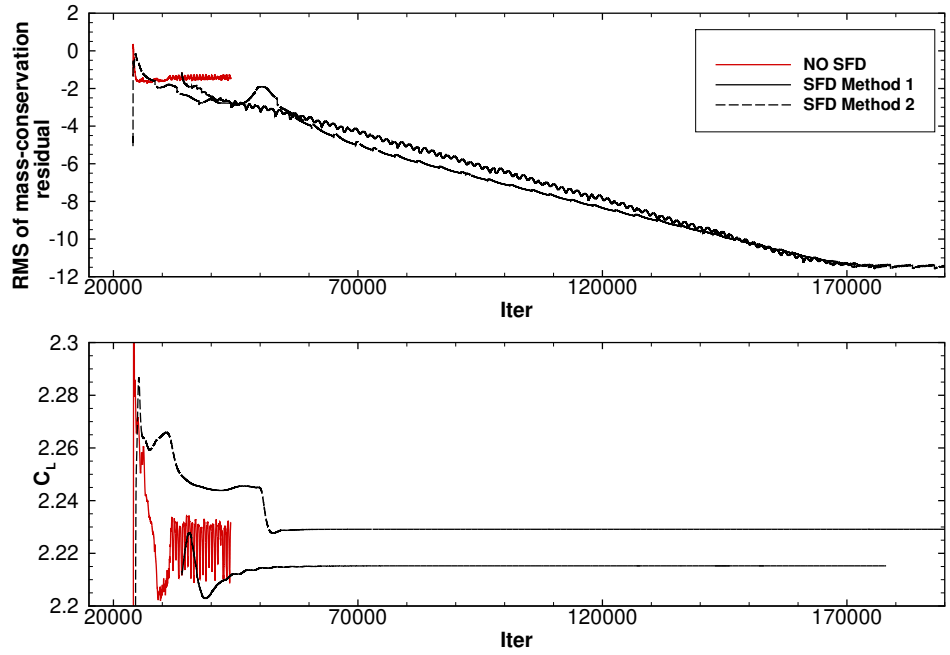

Fig. 21 Test case 3.2 at $\alpha = 16°$: iterative convergence using SFD.

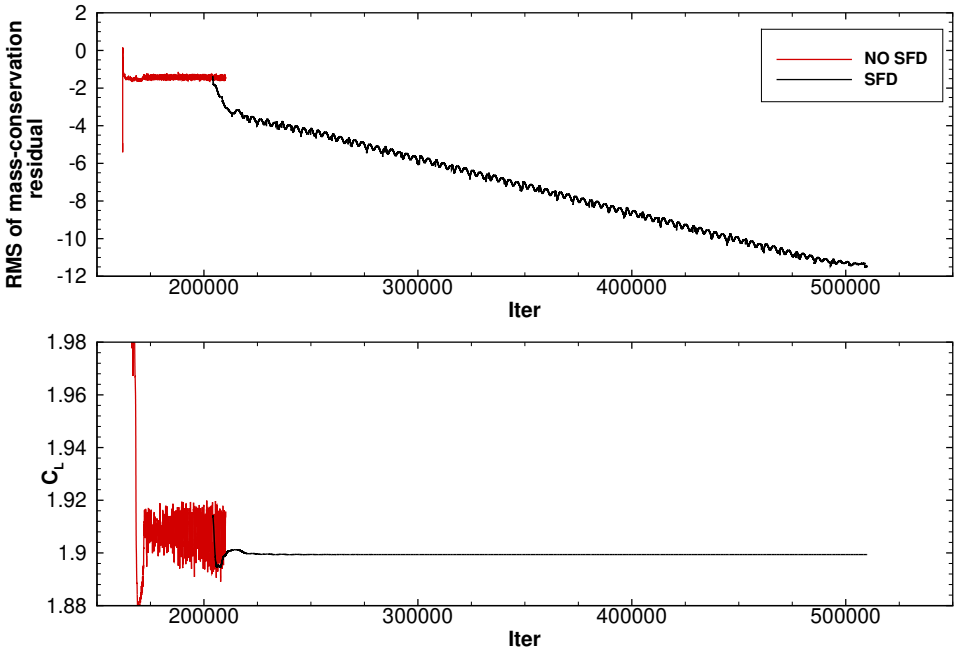

Fig. 22 Test case 3.2 at $\alpha = 20°$: iterative convergence using SFD.

equilibrium state, it may shift into a local minimum near the equilibrium solution and begin oscillating around a mean state that may or may not correspond to the initial equilibrium state. Furthermore, considering the mean value of the limit cycle would be relevant if time-accurate computations were performed, which is not the case here due to the LTS employed in the RANS solver.

Table 2 Converged and mean aerodynamic coefficients over limit cycles for Test case 3.2.

Angle of Attack		C_L	C_D	C_{MY}
6°	Mean Value	1.618920	0.1759978	-0.3353656
	SFD Value	1.618916	0.1759987	-0.3353641
16°	Mean Value	2.225092	0.3286236	-0.1857690
	SFD Value	2.215250	0.3342033	-0.1635082
20°	Mean Value	1.908154	0.4461614	-0.1375233
	SFD Value	1.899386	0.4499997	-0.1170122

Two distinct methods were employed to apply the SFD. The first one, referred to in this work as Method 1, waits for the limit cycles to develop and then applies the SFD with a given set of parameters. The second one, referred to in this work as Method 2, applies the SFD directly at the first iteration using the same set of parameters. Both methods are started from the converged solution of the previous angle of attack at $\alpha = 6°$, corresponding to a warm start. Interestingly, modifying the moment at which the SFD is applied results in different converged steady-state solutions of the RANS equations, as displayed in Fig. 21. The differences in the drag and pitching moments are displayed in Fig.

B2 in Appendix, and a summary of the different aerodynamic coefficients obtained is presented in Table 3. This can be interpreted as a modification of the initialization method, one using a classical warm start, the other employing an SFD-warm-start. This observation was already hinted at by Plante and Laurendeau [31] during HLPW4, who witnessed different limit cycles when employing different restart methods. In their work, they claimed that "The two methods for warm-start change the limit cycle that is obtained. If the solutions were converged, one could argue that there are multiple solutions to the RANS equations." Here, being able to converge both initialization methods 1 and 2 leads us to this conclusion: there are multiple converged solutions to the numerical RANS equations with the spatial discretization used in this work, which relies on a non-grid-converged mesh.

Table 3 Test case 3.2 at 16°: aerodynamic coefficients from methods 1 and 2.

	C_L	C_D	C_{MY}
Method 1	2.21525	0.33420	-0.16351
Method 2	2.22913	0.33716	-0.15796

To better understand where this difference in the aerodynamic coefficients comes from, the surface skin-friction coefficients of the converged solutions for Method 1 and Method 2 are plotted in Fig. 23. Moreover, the difference is plotted next to each other to highlight the regions where the skin friction are different. The differences are not observed in the pizza-slice areas, but instead around the engine and its wake. When restarting the flow directly with the SFD enabled, a larger separation is observed on the engine. It also appears that the inboard flap separates earlier.

It is important to note that observations of the steady-state converged surface plots in Fig. 23 reveal that the SFD method did not resolve the pizza-slice problem. These patterns did not disappear under the effect of SFD, although the oscillations previously observed in their vicinity are no longer present. However, as discussed in the previous paragraph, SFD has demonstrated the potential to converge solutions obtained from different restart methods. Given that our solutions are deeply converged, the remaining discrepancies can likely be attributed to other factors, such as discretization or turbulence modeling errors. Nevertheless, it is believed that SFD has its role to play in the sense that it shall help to stabilize any RANS solver to converge to a steady state, regardless of the initial conditions.

Finally, it was shown here that SFD is effective on a complex geometry, namely the Wing-Body-Slat-Flap-Nacelle geometry, even at high angles of attack after the maximum lift. Therefore, it is hypothesized that, given a mesh prepared under meshing best practices,the iterative convergence issues encountered for simpler geometries such as those of Test Cases 2.2 and 2.3 can be handled using the SFD.

V. Conclusion

This paper presents the application of the CHAMPS flow solver to test cases from the Fifth AIAA CFD High-Lift Prediction Workshop (HLPW5), with an emphasis on achieving deep convergence using the Selective Frequency

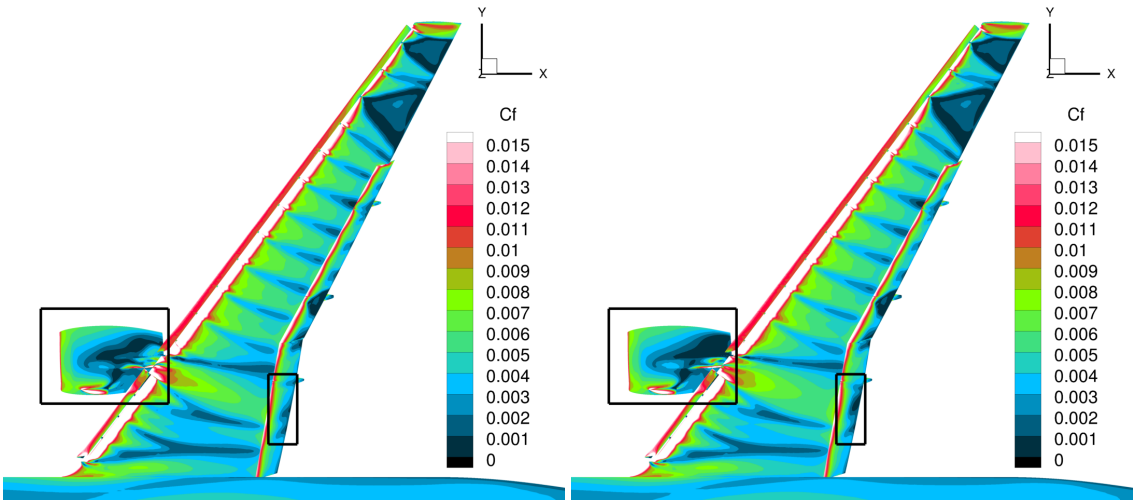

(a) **(b)**

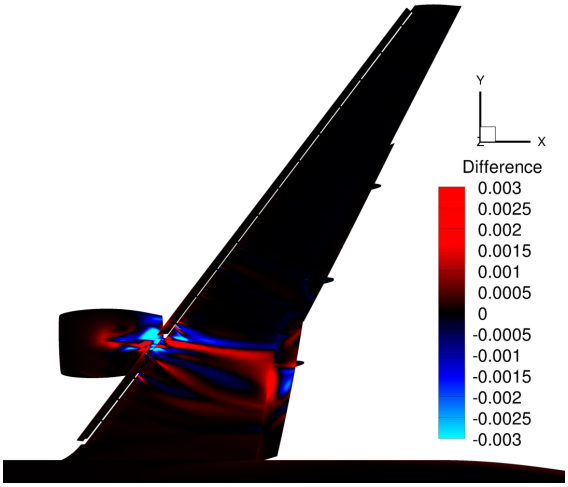

(c)

Fig. 23 Skin friction at 16° **for case 3.2: a) standard restart, b) SFD-restart, c) difference between both.**

Damping (SFD) method. Observations and analyses of the HLPW5 results highlight the presence of limit cycles encountered by many Reynolds-Averaged Navier-Stokes (RANS) solvers. These limit cycles are linked to pseudo-unsteady phenomena occurring on the aircraft's surface and have been identified as the primary factor preventing RANS solvers from reducing residuals to low levels. The SFD method was introduced to improve iterative convergence of RANS solvers for HLPW5 configurations. By carefully selecting the SFD input parameters, converged solutions were obtained for complex high-lift flows. Furthermore, it was shown that multiple solutions of the numerical RANS equations on a non-grid converged mesh can be obtained, depending on the restart strategy employed. Finally, despite the use of the SFD method, large spurious separation areas—responsible for significant discrepancies in aerodynamic coefficients for RANS solvers are still present even in the low-residual high-lift flow solutions, which cannot be attributed to a lack of residual convergence of the steady state solver.

Appendix A: Separation regions

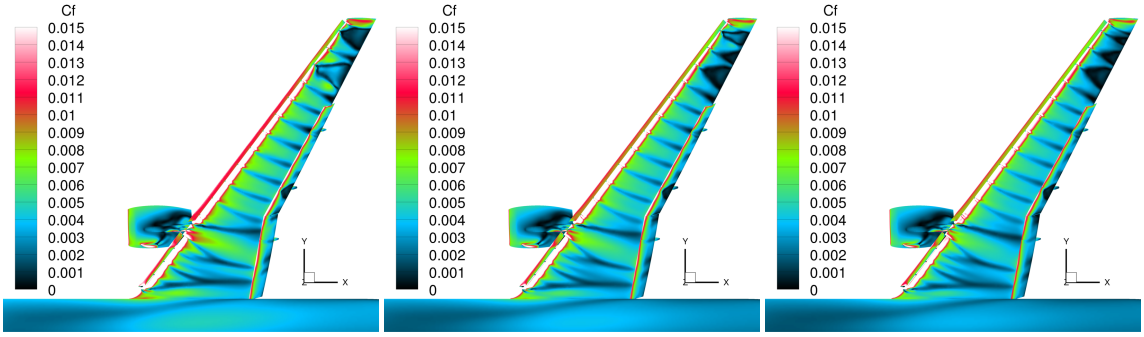

(a) $\alpha = 16°$, **TC3.2;** **(b)** $\alpha = 16°$, **TC3.3;** **(c)** $\alpha = 16°$, **TC3.4;**

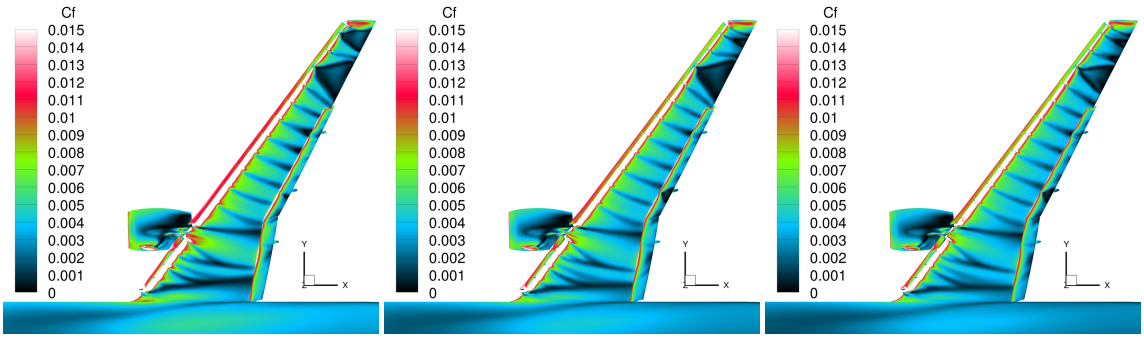

(d) $\alpha = 18°$, **TC3.2;** **(e)** $\alpha = 18°$, **TC3.3;** **(f)** $\alpha = 18°$, **TC3.4;**

(g) $\alpha = 20°$, **TC3.2;** **(h)** $\alpha = 20°$, **TC3.4;**

(i) $\alpha = 22°$, **TC3.2;** **(j)** $\alpha = 22°$, **TC3.4;**

Fig. A1 Skin friction coefficient evolution with α: Cases 3.2 (left), 3.3 (middle), 3.4 (right).

Appendix B: Coefficient Convergence Comparison

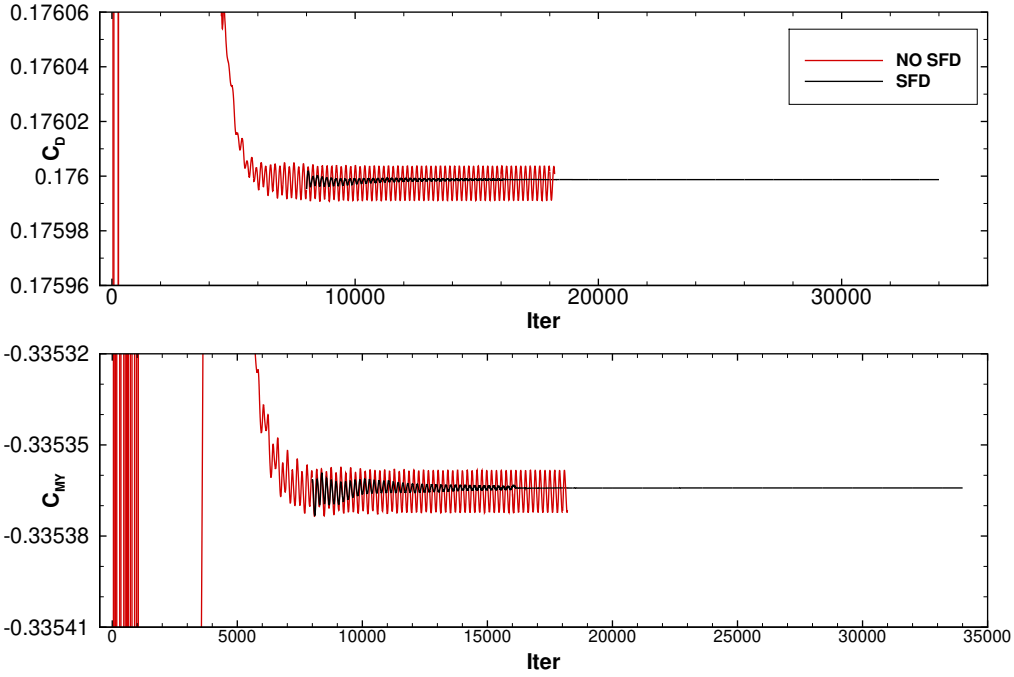

Fig. B1 Test case 3.2 at 6°: drag and pitching moment iterative convergence with and without SFD

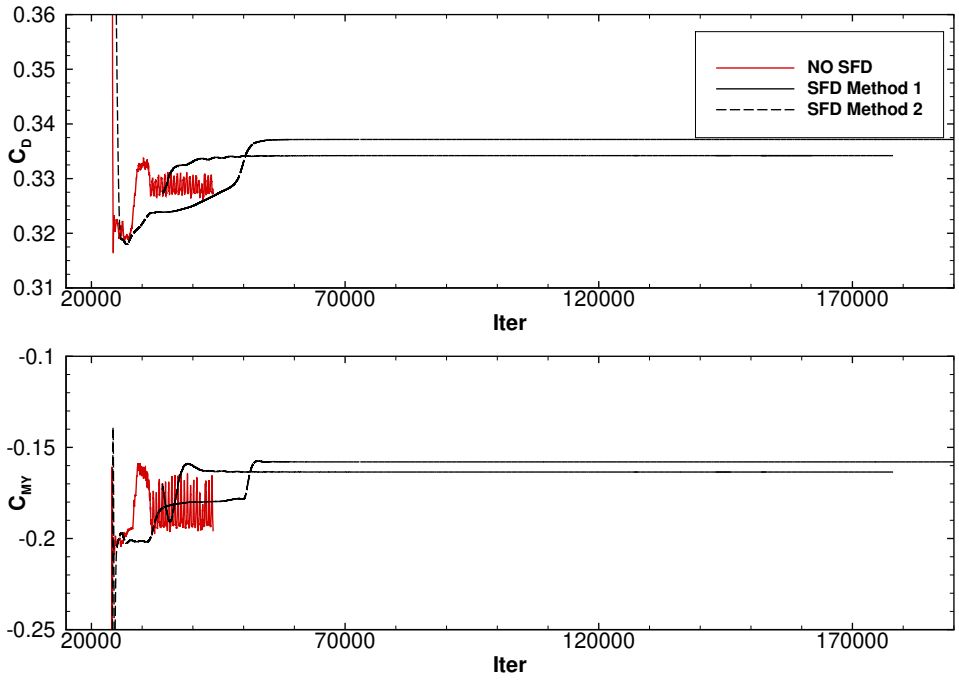

Fig. B2 Test case 3.2 at 16°: drag and pitching moment iterative convergence with and without SFD, using two initialization methods.

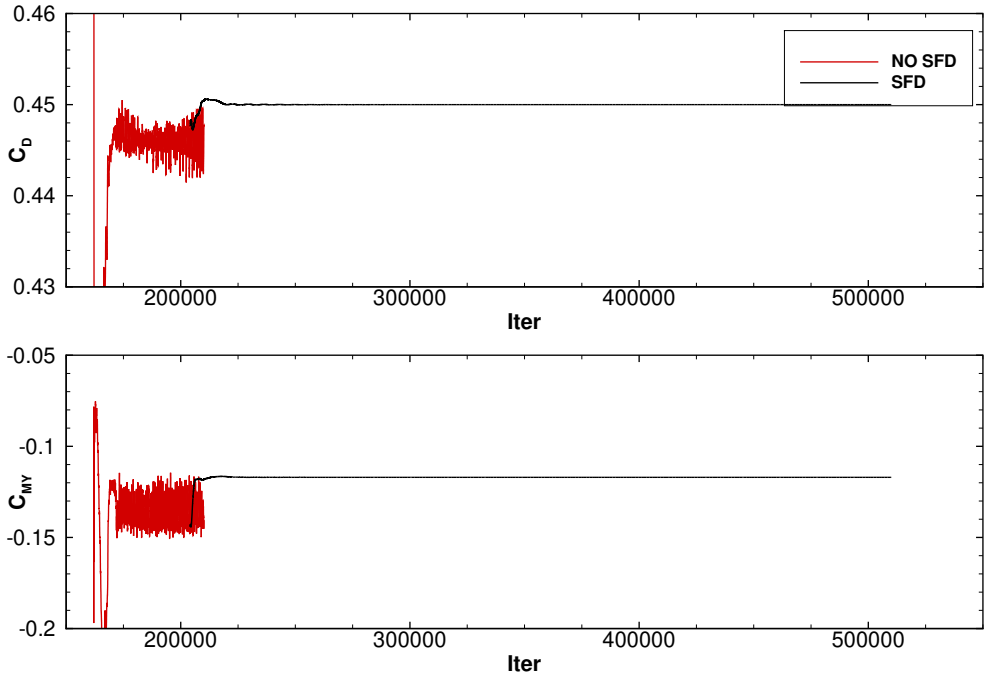

Fig. B3 Test case 3.2 at 20°: drag and pitching moment iterative convergence with and without SFD

Funding Sources

This work is supported in part by a Bombardier/NSERC/CRIAQ Industrial Chair.

Acknowledgments

The authors acknowledge the Digital Research Alliance of Canada and Calcul Québec for providing the computational resources used in this work.

References

[1] Diskin, B., Rumsey, C. L., Wang, L., and Iyer, P. S., "High-Lift Prediction Workshop 5: Fixed-Grid Reynolds-Averaged Navier–Stokes Technology Focus Group Summary," *AIAA SCITECH 2025 Forum*, 2025. https://doi.org/10.2514/6.2025-0046.

[2] Arnould, B., and Éric Laurendeau, "CHAMPS' Fixed Grid RANS Simulations at Fifth High Lift Prediction Workshop," *AIAA SCITECH 2025 Forum*, 2025. https://doi.org/10.2514/6.2025-0279.

[3] Mouton, S., Charpentier, G., and Lorenski, A., "Test Summary of the Full-Span High-Lift Common Research Model at the ONERA F1 Pressurized Low-Speed Wind Tunnel," *AIAA SCITECH 2023 Forum*, 2023. https://doi.org/10.2514/6.2023-0823.

[4] Crouch, J., Garbaruk, A., and Magidov, D., "Predicting the onset of flow unsteadiness based on global instability," *Journal of Computational Physics*, Vol. 224, No. 2, 2007, pp. 924–940. https://doi.org/https://doi.org/10.1016/j.jcp.2006.10.035.

[5] Crouch, J. D., Garbaruk, A., and Strelets, M., "Global instability in the onset of transonic-wing buffet," *Journal of Fluid Mechanics*, Vol. 881, No. A, 2019, p. 3–22. https://doi.org/10.1017/jfm.2019.748.

[6] Plante, F., Dandois, J., Beneddine, S., Laurendeau, , and Sipp, D., "Link between subsonic stall and transonic buffet on swept and unswept wings: from global stability analysis to nonlinear dynamics," *Journal of Fluid Mechanics*, Vol. 908, No. A, 2021, p. A16. https://doi.org/10.1017/jfm.2020.848.

[7] Parenteau, M., Bourgault-Cote, S., Plante, F., Kayraklioglu, E., and Laurendeau, E., "Development of Parallel CFD Applications with the Chapel Programming Language," *AIAA Scitech 2021 Forum*, 2021. https://doi.org/10.2514/6.2021-0749.

[8] Chamberlain, B., Callahan, D., and Zima, H., "Parallel Programmability and the Chapel Language," *Int. J. High Perform. Comput. Appl.*, Vol. 21, No. 3, 2007, p. 291–312. https://doi.org/10.1177/1094342007078442.

[9] Venkatakrishnan, V., "Convergence to Steady State Solutions of the Euler Equations on Unstructured Grids with Limiters," *Journal of Computational Physics*, Vol. 118, No. 1, 1995, pp. 120–130. https://doi.org/https://doi.org/10.1006/jcph.1995.1084.

[10] SPALART, P., and ALLMARAS, S., "A one-equation turbulence model for aerodynamic flows," *30th Aerospace Sciences Meeting and Exhibit*, 1992. https://doi.org/10.2514/6.1992-439.

[11] Mavriplis, D. J., and Jameson, A., "Multigrid solution of the Navier-Stokes equations on triangular meshes," *AIAA Journal*, Vol. 28, No. 8, 1990, pp. 1415–1425. https://doi.org/10.2514/3.25233.

[12] Åkervik, E., Brandt, L., Henningson, D. S., Hœpffner, J., Marxen, O., and Schlatter, P., "Steady solutions of the Navier-Stokes equations by selective frequency damping," *Physics of Fluids*, Vol. 18, No. 6, 2006, p. 068102. https://doi.org/10.1063/1.2211705.

[13] Ilak, M., Schlatter, P., Bagheri, S., and Henningson, D. S., "Bifurcation and stability analysis of a jet in cross-flow: onset of global instability at a low velocity ratio," *Journal of Fluid Mechanics*, Vol. 696, No. A, 2012, p. 94–121. https://doi.org/10.1017/jfm.2012.10.

[14] NICHOLS, J. W., and SCHMID, P. J., "The effect of a lifted flame on the stability of round fuel jets," *Journal of Fluid Mechanics*, Vol. 609, No. A, 2008, p. 275–284. https://doi.org/10.1017/S0022112008002528.

[15] Qadri, U. A., Chandler, G. J., and Juniper, M. P., "Self-sustained hydrodynamic oscillations in lifted jet diffusion flames: origin and control," *Journal of Fluid Mechanics*, Vol. 775, No. A, 2015, p. 201–222. https://doi.org/10.1017/jfm.2015.297.

[16] PIER, B., "Local and global instabilities in the wake of a sphere," *Journal of Fluid Mechanics*, Vol. 603, No. A, 2008, p. 39–61. https://doi.org/10.1017/S0022112008000736.

[17] Pier, B., and Peake, N., "Global nonlinear dynamics of thin aerofoil wakes," *Seventh IUTAM Symposium on Laminar-Turbulent Transition*, edited by P. Schlatter and D. S. Henningson, Springer Netherlands, 2010, pp. 319–324. https://doi.org/https://doi.org/10.1007/978-90-481-3723-7_51.

[18] Moise, P., "Bistability of bubble and conical forms of vortex breakdown in laminar swirling jets," *Journal of Fluid Mechanics*, Vol. 889, No. A, 2020, p. A31. https://doi.org/10.1017/jfm.2020.105.

[19] Jordi, B. E., Cotter, C. J., and Sherwin, S. J., "Encapsulated formulation of the selective frequency damping method," *Physics of Fluids*, Vol. 26, No. 3, 2014, p. 034101. https://doi.org/10.1063/1.4867482.

[20] Casacuberta, J., Groot, K. J., Tol, H. J., and Hickel, S., "Effectivity and efficiency of selective frequency damping for the computation of unstable steady-state solutions," *Journal of Computational Physics*, Vol. 375, No. A, 2018, pp. 481–497. https://doi.org/https://doi.org/10.1016/j.jcp.2018.08.056.

[21] Plante, F., Dandois, J., and Laurendeau, E., "Similarities Between Cellular Patterns Occurring in Transonic Buffet and Subsonic Stall," *AIAA Journal*, Vol. 58, No. 1, 2020, pp. 71–84. https://doi.org/10.2514/1.J058555.

[22] Bengana, Y., Loiseau, J.-C., Robinet, J.-C., and Tuckerman, L. S., "Bifurcation analysis and frequency prediction in shear-driven cavity flow," *Journal of Fluid Mechanics*, Vol. 875, No. A, 2019, p. 725–757. https://doi.org/10.1017/jfm.2019.422.

[23] Pini, A., Cammi, A., Lorenzi, S., Cauzzi, M., and Luzzi, L., "A CFD-based simulation tool for the stability analysis of natural circulation systems," *Progress in Nuclear Energy*, Vol. 117, No. A, 2019, p. 103093. https://doi.org/https://doi.org/10.1016/j.pnucene.2019.103093.

[24] Rodríguez, D., Gennaro, E. M., and Souza, L. F., "Self-excited primary and secondary instability of laminar separation bubbles," *Journal of Fluid Mechanics*, Vol. 906, No. A, 2021, p. A13. https://doi.org/10.1017/jfm.2020.767.

[25] Plante, F., and Éric Laurendeau, "Acceleration of Euler and RANS solvers via Selective Frequency Damping," *Computers Fluids*, Vol. 166, No. A, 2018, pp. 46–56. https://doi.org/https://doi.org/10.1016/j.compfluid.2018.01.027.

[26] Paladini, E., Marquet, O., Sipp, D., Robinet, J.-C., and Dandois, J., "Various approaches to determine active regions in an unstable global mode: application to transonic buffet," *Journal of Fluid Mechanics*, Vol. 881, No. A, 2019, p. 617–647. https://doi.org/10.1017/jfm.2019.761.

[27] Zauner, M., Sansica, A., Matsuzaki, T., James Lusher, D., and Hashimoto, A., "Free-Air Simulation Sensitivities on NASA's High-Lift Common Research Model," *AIAA Journal*, Vol. 63, No. 6, 2025, pp. 2224–2248. https://doi.org/10.2514/1.J064511.

[28] Liguori, V., Plante, F., and Laurendeau, E., "Implementation of an efficient Selective Frequency Damping method in a RANS solver," *AIAA Scitech 2021 Forum*, 2021. https://doi.org/10.2514/6.2021-0359.

[29] Jordi, B. E., Cotter, C. J., and Sherwin, S. J., "An adaptive selective frequency damping method," *Physics of Fluids*, Vol. 27, No. 9, 2015, p. 094104. https://doi.org/10.1063/1.4932107.

[30] Cunha, G., Passaggia, P.-Y., and Lazareff, M., "Optimization of the selective frequency damping parameters using model reduction," *Physics of Fluids*, Vol. 27, No. 9, 2015, p. 094103. https://doi.org/10.1063/1.4930925.

[31] Plante, F., and Laurendeau, E., "CHAMPS Contributions to the Fourth High Lift Prediction Workshop," *AIAA AVIATION 2022 Forum*, 2022. https://doi.org/10.2514/6.2022-3744.